ANL-ART-150

Development of a Mechanistic Thermal Aging Model for Grade 91

Applied Materials Division

About Argonne National Laboratory
Argonne is a U.S. Department of Energy laboratory managed by UChicago Argonne, LLC under contract DE-AC02-06CH11357. The Laboratory's main facility is outside Chicago, at 9700 South Cass Avenue, Argonne, Illinois 60439. For information about Argonne and its pioneering science and technology programs, see www.anl.gov.

DOCUMENT AVAILABILITY

Online Access: U.S. Department of Energy (DOE) reports produced after 1991 and a growing number of pre-1991 documents are available free via DOE's SciTech Connect (http://www.osti.gov/scitech/)

Reports not in digital format may be purchased by the public from the National Technical Information Service (NTIS):

U.S. Department of Commerce
National Technical Information
Service 5301 Shawnee Rd
Alexandria, VA 22312
www.ntis.gov
Phone: (800) 553-NTIS (6847) or (703) 605-6000
Fax: (703) 605-6900
Email: **orders@ntis.gov**

Reports not in digital format are available to DOE and DOE contractors from the Office of Scientific and Technical Information (OSTI):

U.S. Department of Energy
Office of Scientific and Technical Information
P.O. Box 62
Oak Ridge, TN 37831-0062
www.osti.gov
Phone: (865) 576-8401
Fax: (865) 576-5728
Email: **reports@osti.gov**

Disclaimer
This report was prepared as an account of work sponsored by an agency of the United States Government. Neither the United States Government nor any agency thereof, nor UChicago Argonne, LLC, nor any of their employees or officers, makes any warranty, express or implied, or assumes any legal liability or responsibility for the accuracy, completeness, or usefulness of any information, apparatus, product, or process disclosed, or represents that its use would not infringe privately owned rights. Reference herein to any specific commercial product, process, or service by trade name, trademark, manufacturer, or otherwise, does not necessarily constitute or imply its endorsement, recommendation, or favoring by the United States Government or any agency thereof. The views and opinions of document authors expressed herein do not necessarily state or reflect those of the United States Government or any agency thereof, Argonne National Laboratory, or UChicago Argonne, LLC.

ANL-ART-150

Development of a Mechanistic Thermal Aging Model for Grade 91

Meimei Li, Weiying Chen, K. Natesan
Applied Materials Division
Argonne National Laboratory

August 2018

ABSTRACT

This report provides a summary on understanding and predicting the effects of long-term thermal aging on microstructure and tensile properties of G91 to corroborate the ASME Code rules in strength reduction due to elevated temperature service. The research is to support the design and long-term operation of G91 structural components in sodium-cooled fast reactors (SFRs). The report is a Level 2 deliverable in FY18 (M2NT-18AN050502061), under the Work Package NT-18AN05050206, "G91 Code Extension Testing" performed by the Argonne National Laboratory (ANL), as part of the Advanced Materials Development Program for Fast Reactors.

The thermal aging study of G91 involves three types of thermally-aged specimens: (1) specimens machined from two heats of G91, G91-H1 and H30176 that have been tested for the Advanced Materials Development Programs in the past years. These specimens were aged at 550, 600, and 650°C for times up to ~64,000 h; (2) specimens fabricated from the heads of the archived crept specimens (13 in total) of six heats of G91, H5349, H30394, H30383, H10148, H30176. These specimens were aged at 427 - 538°C and for times up to 132,647 h; (3) specimens made from a tube removed from the Kingston coal-fired power plant after exposure for 155,000 h at 550°C. These three sets of specimens provide a comprehensive data set for understanding and predicting the effect of long-term thermal aging on microstructure and tensile properties of G91.

Microstructural analysis of the thermally-aged G91 revealed that thermal aging causes significant microstructural changes: (1) the tempered martensite formed during tempering is unstable, and suffers significant recovery during aging, manifested by an increase in subgrain width, a decrease in subgrain length, and a decrease in subgrain aspect ratio (i.e. subgrains become more equiaxed) as the aging temperature and time increase. The subgrain recovery is facilitated by the reduction of dislocation density within subgrains; (2) $M_{23}C_6$ carbides in the as-received G91 are distributed along grain and subgrain boundaries and play an important role as pinning obstacles against subgrain coarsening. $M_{23}C_6$ carbides coarsen during aging, and the coarsening of $M_{23}C_6$ carbides reduces the pinning force on the boundaries; (3) MX carbonitrides in the as-received G91 are distributed uniformly within subgrains, providing the precipitation hardening effect. They coarsen with increasing aging temperature and time, but the coarsening rate is low; (3) a new phase, the Laves phase intermetallic forms during aging. The formation of the Laves phase removes the Mo solutes from the matrix, reducing the solid solution strengthening effect. The Laves phase particles grow rapidly once they are nucleated, and they precipitate primarily along boundaries. They may have a pinning effect on boundaries, but should provide little to the alloy strength. The evolution of each microstructural constituent during thermal aging can be well described by individual microstructural models. The estimated activation energy for MX coarsening was 175 kJ/mol, equivalent to the activation energy for boundary and core diffusion in α-Fe, while the estimated activation energy for subgrain coarsening was significantly lower, ~96 kJ/mol.

Thermal aging of G91 results in the reduction in the yield stress and the ultimate tensile strength but has an insignificant effect on the uniform and total elongations. The reduction in tensile strength is more pronounced as the aging temperature and time increases. The *in situ* tensile tests with high-energy X-rays revealed that sub-boundary strengthening plays a dominant role, and the strengthening role of $M_{23}C_6$ particles may be accounted for by subgrian boundary hardening,

and three strengthening mechanisms can be superimposed to describe the tensile strength of G91: subgrain boundary hardening, MX precipitation hardening, and Mo solid solution strengthening. A microstructure – strength model was established to describe the effect of thermal aging on the yield and tensile strength of G91. The calculated yield stress – aging time and ultimate tensile strength – aging time curves shows an excellent agreement with the experimental data. The model was then used to predict the yield and tensile strength reduction factors for thermally-aged G91 for the aging temperatures of 500 - 650°C with a 25°C interval for times up to 1×10^6 h (114 yr). The predicted values were compared with the yield and tensile strength reductions factors for times up to 3×10^5 h (34 yr) for G91 in ASME B&PV Code Section III, Subsection NH (new Division 5) Table NH-3225-2 and Table NH-3225-4. The predicted values are generally lower than the ASME Code values, and the differences become more significant at higher temperatures and longer times. It was predicted that G91 can retain ~70% of its initial tensile strength at the end life of 1×10^6 h at the service temperature of 500°C.

TABLE OF CONTENTS

LIST OF TABLES

LIST OF FIGURES

1 Introduction

Advanced materials are a key element in the development of advanced nuclear reactors. High-performance structural materials allow for a compact and simple design of the reactor structure, and have the potential to reduce the construction and operational costs for next-generation nuclear energy systems. High temperature-, corrosion- and irradiation-resistant alloys are important for flexible, reliable and safe designs of reactor components.

Advanced fast reactors will operate at higher temperatures than current light water reactors (LWRs). The design of high-temperature structural components must consider time-dependent effects and damage mechanisms, such as long-term thermal aging, creep, creep-fatigue, creep ratcheting, and environmental effects. These issues have not been dealt with in LWR designs and operation. Due to the temperature and time dependence of material properties, extrapolation of short-term, high-temperature accelerated test data to a long-design life and a relatively low-service temperature becomes extremely difficult and often with large uncertainties. Nuclear components that operate at elevated temperatures must be designed in accordance with the American Society of Mechanical Engineers (ASME) Section III Division 5 (previously Subsection NH – Class 1 Components in Elevated Temperature Service), which provides high temperature design rules for structural components in nuclear service. Materials that are allowed for use in high-temperature structural designs in nuclear components must be qualified and approved by Division 5. So far only five materials have been qualified, namely, Type 304 and 316 austenitic stainless steels, 2.25Cr-1Mo steel, modified 9Cr-1Mo (Grade 91) steel, and Alloy 800H. Alloy 617 is being qualified for inclusion in Division 5.

Grade 91 (G91) ferritic-martensitic steel was developed for intermediate heat exchanger and steam generator applications for liquid metal reactors (LMRs) in the U.S in late 1970s. In 1974, the U.S. Department of Energy (DOE) initiated a three-phase study for developing a new alloy for use in LMRs, and G91 was selected based on creep strength and microstructural considerations. A development program for G91 steel started in early 1980s, and considerable information on G91 was generated through the DOE-sponsored programs and industrial development. An extensive mechanical properties database was established in air environment, including tensile, toughness, creep, and fatigue properties. Some creep-fatigue data were also obtained, but were considered insufficient. The general findings were that the alloy has good long-term performance for structural applications in LMRs, and is resistant to irradiation swelling. Data in sodium showed no significant deleterious effects on mechanical properties. One of the remaining critical issues to be resolved is the long-term performance of G91 in the sodium-cooled fast reactor (SFR) environments including thermal aging, sodium exposure and neutron irradiation. G91 is a multi-component, multi-phase alloy with much more complex microstructure than other four Code-qualified single-phase alloys. The superior high-temperature performance of G91 heavily relies on the stability of its complex microstructure. Significant microstructural changes can occur during long-term thermal aging, leading to dramatically different responses to the service environment. Extrapolation of short-term, laboratory-generated data to design allowable stresses for higher temperatures and extended service lives must be conducted with sufficient confidence to ensure the safety and reliability of structural components in sodium-cooled fast reactors.

The goal of this project is to develop a mechanistic approach to address the long-term thermal aging effect on tensile strength for the 60-year design life. This report presents the microstructure – tensile strength model and the predictions of the strength reduction factors due to long-term elevated temperature service for G91 steel. The yield and tensile strength reduction factors for thermally-aged G91 were calculated for aging times up to 1,000,000 h (114 y) in the temperature range of 500 - 650°C with a 25°C interval. The predicted values were compared with the currently available ASME Code recommendations for times up to 300,000 h (34 y).

2 Experimental Procedure and Modeling Approaches

2.1 Thermal aging experiments

Thermal aging experiments were conducted on two heats of G91 steel, i.e., G91-H1 and H30176. The aging temperatures were 550, 600, and 650°C, and the maximum aging time was ~64,000 h. These experiments were designed to obtain a comprehensive dataset covering a range of aging temperatures and exposure times with controlled metallurgical variations.

Heat G91-H1 was in plate form with a thickness of 0.375". The plate was normalized at 1050°C for 1 h, air cooled, and tempered at 760°C for 1 h, air cooled. Heat H30176 of G91 was in 1"-thick plate form. It was normalized at 1050°C for 1 h, air cooled, and tempered at 760°C for 2 h, air cooled. The chemical composition and heat treatment conditions of these two heats are given in Tables 1 and 2, respectively.

Table 1. Chemical composition (in wt%) for G91-H1 and H30176.

Heat No.	Fe	C	Cr	Mn	Mo	N	Nb	Si	V	W
G91-H1	Bal	0.09	8.3	0.46	1.04	0.06	0.05	0.41	0.22	-
H30176	Bal	0.08	8.6	0.37	0.89	0.06	0.07	0.11	0.21	<0.01

Table 2. Heat treatment conditions for G91-H1 and H30176.

Heat No.	Heat treatment
G91-H1	Normalized at 1050°C and tempered at 760°C for 1 h and AC
H30176	Normalized at 1050°C for 1 h, AC, and tempered at 760°C for 2 h, AC

Subsize sheet-type tensile specimens with extended grip sections (Fig. 1) were used in thermal aging experiments, post-exposure microstructural analysis and tensile tests. The design of extended grip sections was to ensure that microstructural characterization and tensile tests can be carried out on the sample exposed to the same aging environment. The tensile specimens were electrical-discharge-machined with the gage parallel to the rolling direction. The tensile specimen has nominal gage dimensions of 7.62 × 1.52 × 0.76 mm.

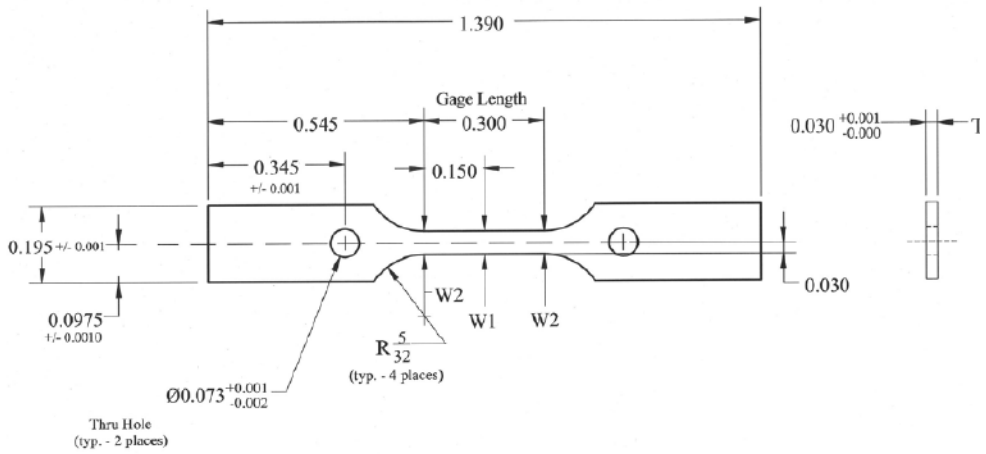

Figure 1. Schematic drawing of subsize sheet-type tensile specimens with extended grip sections for microstructural analysis.

Thermal aging experiments were performed at 550, 600, and 650°C in air furnaces for various exposure times. Each specimen was wrapped in Ta foil and encapsulated in a quartz tube under vacuum. Encapsulated specimens were loaded in an air furnace. Table 3 gives the total exposure times at different temperatures for the two heats of G91.

Table 3. Thermal aging temperatures and total aging times for G91-H1 and H30176.

Heat No.	Total Exposure Time at 550°C (h)	Total Exposure Time at 600°C (h)	Total Exposure Time at 650°C (h)
G91 H1	52,121	64,313	55,277
H30176	42,545	44,639	44,779

2.2 Archived thermally-aged specimens

The Oak Ridge National Laboratory (ORNL) provided us 13 archived G91 creep-tested specimens that were exposed to temperatures of 427-538°C for up to 132,647 h (~15 years). A G91 tube removed from the Kingston coal-fired power plant was also provided. The Kingston tube was exposed to steam condition at 550°C for 155,000 h (~18 years). These materials provided valuable long-term aging data at relevant SFR operating temperatures.

Table 4 lists the heat number and creep test condition for the archived crept specimens. Note that there are five different heats of G91 in Table 1, i.e., H5349, H30394, H30383, H10148, and H30176. Control specimens are available only for Heat 30176.

Subsize sheet-type tensile specimens (Fig. 2) and rod specimens (ϕ3 mm) were machined from the grip sections of the crept specimen, as shown in Fig. 3(a). Tensile specimens were

electrical-discharge-machined with the gage parallel to the creep loading direction. These specimens represent the static aging state under the crept temperature and time. The tensile specimen has nominal gage dimensions of 7.62 × 1.52 × 0.76 mm. The rod specimen has a diameter of 3 mm, and was used for microstructural analysis. The tensile and rod specimens were also machined from the G91 Kingston tube, as shown in Fig. 3(b).

Table 4. List of the G91 creep-tested specimens

Specimen ID	Heat No.	Temperature (°C)	Stress (MPa)	Time (hrs)
20842	5349	538	179	132,647
21822	30394	427	414	114,800
24577	30394	538	166	97,497
24746	30383	482	276	99,542
24899	10148	538	166	82,061
27386	30383	538	207	40,871
23698	30394	427	379	106,523
24351	30394	538	207	57,460
24357	30176	538	207	57,212
24359	30176	538	186	57,109
24749	30394	482	276	83,491
24752	30176	482	276	84,148
24772	10148	482	276	83,126

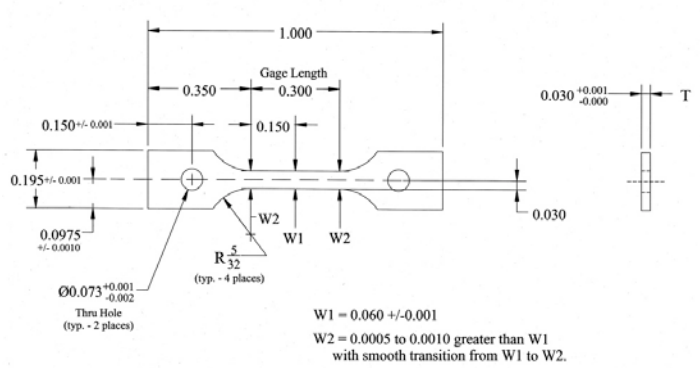

Figure 2. Schematic drawing of the subsize sheet-type tensile specimen machined from the creep-tested specimen.

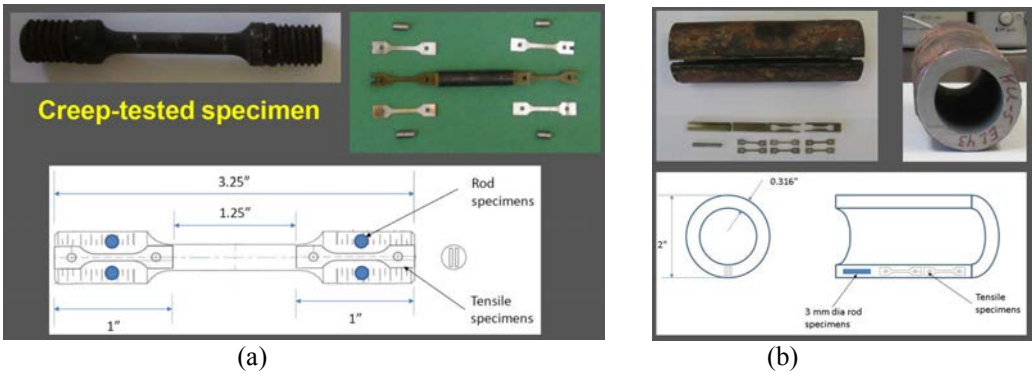

(a) (b)

Figure 3. Fabrication drawings of subsize tensile specimens and rod specimens from (a) an archived G91 creep-tested specimen, and (b) G91 tube removed from the Kingston plant.

2.3 Microstructural characterization

Microstructure of the as-received and thermally-aged specimens was characterized by optical microscopy (OM), high-resolution scanning electron microscopy (SEM), transmission electron microscopy (TEM), energy dispersive spectroscopy (EDS), and synchrotron X-ray diffraction (XRD). Metallographic specimens were prepared by mounting, grinding, and polishing. The polished specimens were chemically etched with an etchant of 5 ml HNO_3, 1 ml HF and 50 ml H_2O. The grain structure of the alloys was revealed by OM. Metallographic specimens were further examined by high resolution SEM to characterize the Laves phase precipitates using both secondary electron (SE) and backscattered electron (BSE) imaging on a field emission gun (FEG) Hitachi S-4700-II microscope. Thin foil TEM specimens of 3-mm in diameter were made by electropolishing to perforation using a Tenupol twin-jet polishing unit. The electropolishing solution was 95% methanol and 5% perchloric acid cooled to about -40°C. TEM and EDS were conducted to examine dislocation density, subgrain structure, and second-phase precipitates. Synchrotron X-ray diffraction was conducted to identify the phases. Subgrains, $M_{23}C_6$ carbides and MX precipitates were analyzed by TEM. Laves phase particles were analyzed by both TEM and SEM.

2.4 Microstructure modeling

Thermal aging-induced subgrain recovery was calculated using the model proposed by Sandstrom [1,2]. According to Sandstrom, subgrain coarsening and growth may occur in two different ways: subgrain boundary migration or subgrain coalescence. Subgrain growth occurs through boundary migration in a similar way as conventional grain growth, and large subgrains grow by consuming smaller ones. Subgrain coalescence occurs by the dissolution of sub-boundaries through three mechanisms: collective migration of sub-boundary dislocations, extraction of sub-boundary dislocations, or emission of sub-boundary dislocations. For subgrain coalescence, the dislocation density in the subgrain interior plays an important role, and the subgrain growth rate is controlled by the recovery of dislocations.

The contribution of extraction of boundary dislocations to the subgrain growth rate, $(dD/dt)_B$ can be described by:

$$\left(\frac{dD}{dt}\right)_B = \frac{M\tau\emptyset\rho h}{\mu} \tag{1}$$

The contribution of emission of boundary dislocations to the subgrain growth rate, $(dD/dt)_e$ is given by:

$$\left(\frac{dD}{dt}\right)_e = \frac{8DM\tau\rho^{1.5}h}{3\mu}\left[exp\left(-\frac{log(2\tau_{up})}{\tau_0\left(1+\left(\frac{\sigma_D}{4\tau_0}\right)^2\right)}\right) - exp\left(-\frac{log(2\tau_{up})}{\tau_0}\right)\right] \tag{2}$$

The contribution of the migration of dislocations in the boundaries (MDB) to the subgrain growth rate, $(dD/dt)_{MDB}$ can be expressed as:

$$\left(\frac{dD}{dt}\right)_{MDB} = \frac{4M\tau}{D} \tag{3}$$

The rate of subgrain growth by sub-boundary migration (BM), $(dD/dt)_{BM}$ is defined as:

$$\left(\frac{dD}{dt}\right)_{BM} = \frac{1.5M\tau}{D} \quad (4)$$

where D is the subgrain diameter, t the time, τ the line tension of the dislocations, and M the dislocation mobility, ρ the dislocation density, h the average distance between dislocations, τ_0 and τ_{up} are related to the dislocation pile-up forces, and ϕ^{-1} is the fraction of subgrain diameter crossed by climb. The effect of alloying elements in solid solution and the presence of second-phase particles can also be accounted for in the subgrain growth models [1,2].

Phase transformation and phase stability in G91 were simulated using the commercial software package Thermo-Calc, DICTRA and TC-PRISMA. Thermo-Calc was used to calculate phase diagrams, chemical compositions, thermodynamic driving force, and amount of equilibrium phases. These thermodynamic data were used as input in the kinetic models to simulate precipitate evolution during thermal aging. DICTRA (Diffusion Controlled TRAnsformation) was used to simulate precipitation kinetics during isothermal aging. DICTRA is a software package for simulation of diffusion-controlled transformation in multicomponent alloys. It is based on a numerical solution of multicomponent diffusion equations in various regions of a material with the assumption of local equilibrium at phase interfaces. The simulation of precipitation kinetics is carried out using the thermodynamic database and the mobility database. The growth of precipitate particles is treated as a one-dimensional moving boundary problem. A local equilibrium is assumed at precipitate and matrix interfaces. The movement of a phase interface is controlled by mass balance obtained from the fluxes of diffusing elements across the interface. The process is controlled by the tendency to reduce the chemical free energy of the system. The contribution of interfacial energy is ignored in the growth model. The precipitate coarsening is simulated using the coarsening model in the DICTRA package. Similar to the growth model, a local equilibrium at phase interfaces is assumed, and the local equilibrium is affected by the interfacial energy. The calculations are performed in a spherical cell with a particle of maximum size at the center of the cell. The maximum size of the particle is assumed to be 1.5 times the size of the average particle size. The largest particle grows at the expense of the smaller particles. At the outer cell boundary, the local equilibrium is defined by the average composition in the system. The effect of grain or subgrain size on phase stability can be evaluated by including grain boundary diffusion. Grain boundary diffusion is implemented in the calculations by assuming that they contribute to the overall diffusion by using the same frequency factor but different activation energy from bulk diffusion. The activation energy for grain boundary diffusion is set by using a predetermined multiplier, and its contribution to the total amount of diffusion is accounted for by using the weighted calculated value for the mobility. Dislocation-assisted diffusion is implemented by assuming that they contributed to the diffusion by using the same frequency factor and different activation energy than that of bulk diffusion. A predetermined multiplier is also used to set the activation energy for dislocation-assisted diffusion and its contribution to the total amount of diffusion is accounted for by using the weighted calculated value for the mobility.

TC-PRISMA is a software package for simulating kinetics of diffusion-controlled multi-particle precipitation process in multi-component and multi-phase alloy systems. It adopts the Kampmann-Wagner numerical (KWN) method [3] to simulate concurrent nucleation, growth, and coarsening of precipitates. The temporal evolution of the mean radius and particle density during the precipitation process is predicted by solving a set of rate equations derived with certain

assumptions for the rates of nucleation and growth as well as the particle size distribution function. TC-PRISMA is integrated with Thermo-Calc and DICTRA to obtain necessary thermodynamic and kinetic data required in the KWN method.

2.5 Ex situ tensile tests and micro-hardness measurements

Ex situ tensile tests were conducted under uniaxial tension at the aging temperature in an air furnace. Figure 4 shows a setup for high temperature tensile tests. Tensile tests were performed in an electromechanical testing system equipped with a three-zone air furnace. The applied load was recorded by a load cell; the specimen displacement was measured by the crosshead extension. The tensile properties were determined from analysis of load versus displacement data files. All the tests were conducted at a nominal strain rate, 0.001 s^{-1}.

Figure 4. Experimental setup for *ex situ* high temperature tensile tests.

Due to a limited number of tensile specimens made from archive crept specimens, micro-hardness measurements were conducted to understand the effect of thermal aging on the room-temperature tensile strength. Micro-hardness tests were conducted on the grip section of the tensile specimen using a Buehler Micromet micro-hardness tester. The applied load was 200 g and the dwell time was 10 s. Five measurements were made on each specimen and the mean values are reported.

2.6 In situ tensile tests with synchrotron high-energy X-rays

In situ tensile tests with high-energy X-ray were performed at the 1-ID beamline at the Advanced Photon Source (APS). Beamline 1-ID is a high-energy (50-130 keV), high-brilliance X-ray scattering facility. It is equipped with an MTS servo-hydraulic test frame, enabling tension,

compression, and cyclic loading; an infrared heating furnace attached to the MTS test frame provides heating capacity up to 1200°C. This facility combines lab-scale mechanical testing capability with *in situ* microstructural characterization using multiple X-ray probes (diffraction/scattering/imaging), permitting simultaneous characterization of microstructure and mechanical behavior of mm-scale specimens. Figure 5 shows a schematic layout of the beamline setup and the MTS test station.

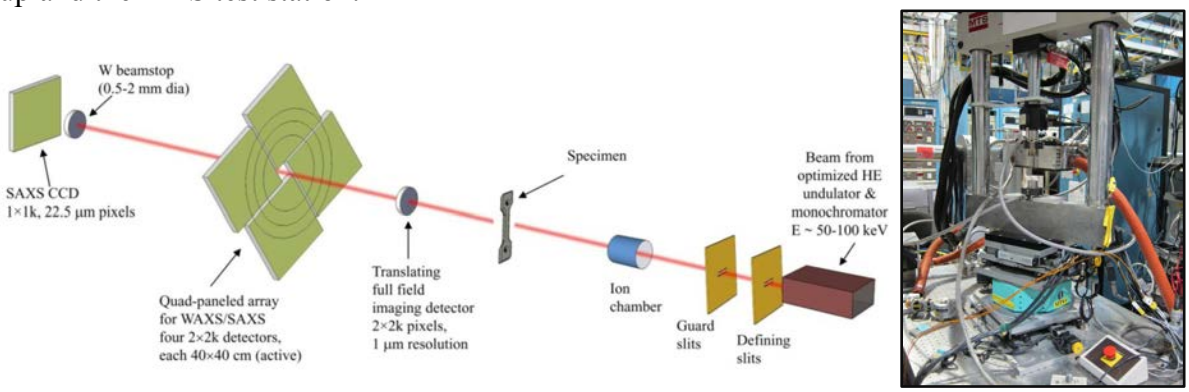

Fig. 5. Schematic layout of Beamline 1-ID and MTS test station at the APS.

In situ uniaxial tensile tests were carried out at 20-650°C in air on the as-received G91 H30176. The tensile tests were carried out under displacement control at a nominal strain rate of 1×10^{-4} s^{-1}. Load and displacement data were recorded, and used to determine the macroscopic stress-strain curve. During tensile deformation, wide- and small-angle X-ray scattering (WAXS/SAXS) measurements were conducted simultaneously with monochromatic X-ray beams in transmission. WAXS signals were obtained at $2° < 2\theta < 20°$, and SAXS at $2\theta < 1°$. Pairs of WAXS and SAXS patterns were independently recorded with a time interval of 14 or 24 s (corresponding to ~0.1 or 0.2% strain), while the specimen was continuously deformed. In addition, the X-ray intensities were measured by two ion chambers before and after the specimen, and these two intensity values were used to calculate the specimen transmission (and therefore the specimen thickness).

Diffraction profiles were obtained from averaging multiple WAXS patterns collected for each measurement. The two-dimensional diffraction data was transformed to one-dimensional line profile (intensity vs. 2θ) by integrating over a $\pm$ 10° azimuth range around the axial/tensile direction of the specimen. Peaks were fitted to pseudo-voigt functions using MATLAB computer programs developed at the 1-ID beamline. Evolution of the lattice strain during tensile deformation was evaluated by calculating the change of the lattice spacing relative to the lattice spacing in the undeformed state. Peak broadening quantified by the full-width at half-maximum (FWHM) of the reflection was analyzed to evaluate the evolution of dislocation density and cell/subgrain structure as a function of tensile strain. The instrumental contribution to peak broadening was calibrated using a LaB_6/CeO_2 sample and subtracted from the measured peak profiles. SAXS data were processed to understand the void formation and evolution at the necking stage.

3 Results

3.1 Effect of thermal aging on microstructure

Grade 91 steel is a multi-component, multi-phase alloy. Figure 6 (a) shows the phase diagram of G91 calculated by Thermo-Calc. There are four stable phases formed at equilibrium at 500-750°C in G91, i.e. bcc-Fe, $M_{23}C_6$ (M = Fe, Cr), Laves phase ($(Fe,Cr)_2Mo$), and Z-phase (Cr(V,Nb)N). In the normalized and tempered condition, the microstructure of G91 consists of three phases, bcc-Fe, $M_{23}C_6$ carbides, and MX (Nb(C,N) or V(N,C)) carbonitrides, identified by X-ray diffraction (XRD), shown in Fig. 7. MX is a metastable phase, shown in Fig. 6(b) where the phase diagram was calculated by suppressing the Z-phase formation.

The bcc-Fe matrix in normalized and tempered (N&T) G91 is tempered martensite consisting of elongated subgrains with a high density of dislocations. Martensite structure is stabilized by $M_{23}C_6$ carbides distributed along boundaries, giving rise to dislocation hardening and subgrain boundary strengthening. MX precipitates are uniformly distributed within subgrains, providing precipitation strengthening. The Mo solutes in the matrix provide additional solid solution strengthening. The maintenance of these microstructural features is critical to the superior high-temperature performance of G91. However, the microstructure of G91 is highly sensitive to chemistry, processing, heat treatment, and service conditions. Detailed microstructural analysis was conducted on thermally-aged G91 specimens to understand the effect of long-term thermal aging on microstructure. The following sections report the findings of microstructural analysis and modeling for G91 thermally-aged at 482 - 650°C.

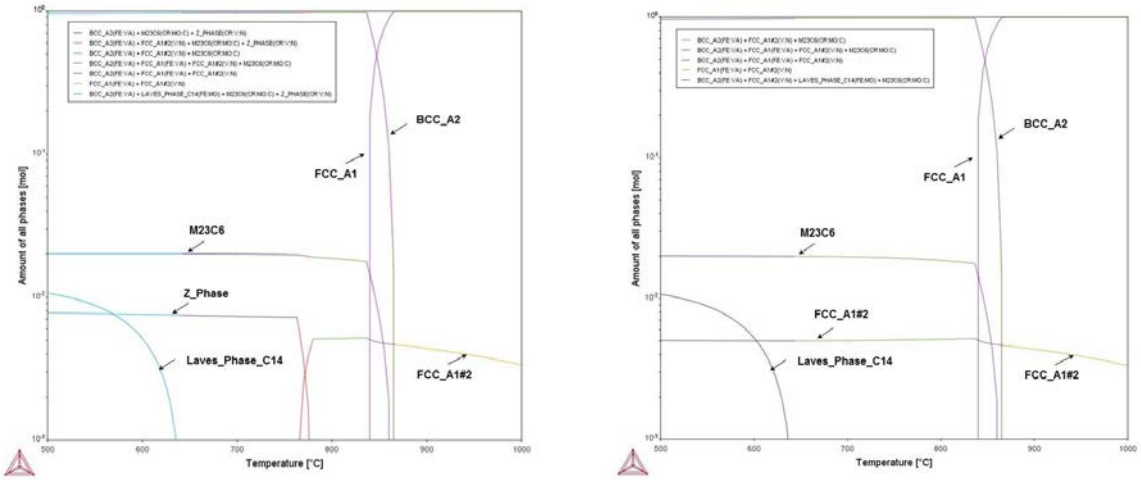

(a) (b)

Figure 6. The calculated phase diagrams of G91 steel with (a) stable phase, Z-phase and (b) metastable phase, MX.

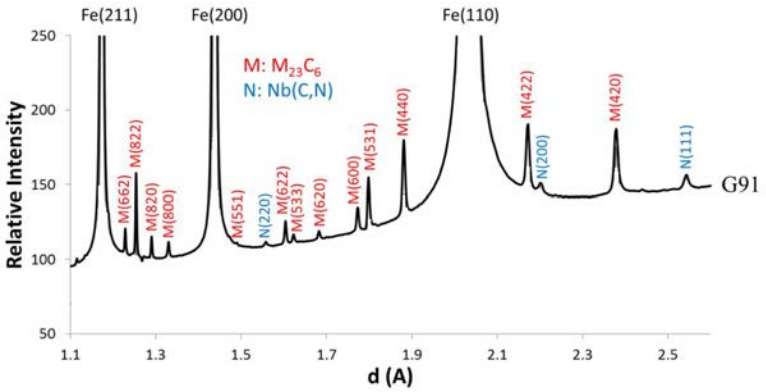

Figure 7. The XRD line profile showing three phases, bcc-Fe, $M_{23}C_6$ and MX in the normalized and tempered G91-H30176.

3.1.1 Dislocation evolution and subgrain recovery

Thermal aging of G91 causes a reduction of dislocation density and subgrain recovery. Subgrain structure and dislocations within subgrains were characterized by TEM. Dislocation densities and subgrain dimensions (width and length) and shape (aspect ratio) were measured with the Image-J software. The dislocation density was estimated by measuring the number of intersections that dislocations make with the grid lines on a TEM micrograph.

Figure 8 shows TEM images of subgrains and distributions of subgrain width, length, aspect ratio, and dislocation density distributions in G91-H1 and H30176 in the as-received condition. The same sets of microstructural data for the G91-H1 specimens thermally aged at 550°C for 19,926 and 52,121 h are given in Figs. 9 (a) and (b), respectively. The thermally-aged specimens show slight increases in subgrain width, decreases in subgrain length, and subgrains became more equiaxed (a smaller subgrain aspect ratio) after aging at 550°C.

Figures 10 (a) and (b) show TEM images of subgrains and distributions of subgrain width, length, aspect ratio, and dislocation density distributions in G91-H30176 after thermal aging at 600°C for 19,992 h, and G91-H1 after aging at 600°C for 40,151 h, respectively. Compared with the as-received G91-H30176 and G91-H1, increases in subgrain width, decreases in subgrain length and decreases in aspect ratio were observed during thermal aging at 600°C.

The effect of thermal aging on microstructural evolution is more pronounced at 650°C. As shown in Figs. 11 (a) and (b) where the subgrain structure and distributions of subgrain width, length, aspect ratio, and dislocation density are shown for G91-H1 after thermal aging at 650°C for 20,531 and 55,277 h, respectively, more significant increases in subgrain width and decreases in subgrain length and aspect ratio and reductions in dislocation density were observed under aging at 650°C. The subgrain size distributions are broadened toward larger values, and the subgrain aspect ratio distributions are narrower towards lower values.

The effect of thermal aging on microstructure at relatively lower temperatures (482 - 538°C) for very long times was investigated by examining the heads of the archived crept specimens. Figures 12 and 13 show TEM micrographs of subgrain structure and distributions of subgrain width, length, aspect ratio and dislocation density for the specimens, ID 20842 (Heat 5349 aged for 132,647 h at 538°C) and ID 24746 (Heat 30383 aged for 99,542 h at 482°C), respectively. Due to the sensitivity of G91 microstructure to the heat variation, processing history, and final heat treatment, and there were no control specimens (pre-aged specimens) for these archived specimens, it is somewhat difficult to draw a clear conclusion on the effect of aging on microstructural evolution from these lower aging-temperature specimens. However, the general trends of subgrain and dislocation evolution remain consistent with the observations in the G91 H1 and H30176 specimens thermally aged at 550-650°C.

The G91 Kingston pipe provides the thermal aging data with the longest aging time at 550°C. As shown in Fig. 14, the microstructural recovery in the martensite matrix continues with increasing aging time.

Figure 15 summarizes the subgrain parameters (width, length and aspect ratio) as a function of aging time for various heats of G91 thermally aged at 538-650°C. While there is a significant data scatter from different heats, it is evident that as the aging temperature and time increase, the subgrain width increases, the subgrain length decreases, and the subgrain aspect ratio decreases (i.e. more equiaxed). There is an apparent incubation period before the onset of aging-induced subgrain recovery, and the incubation time is somewhat dependent on the aging temperature. Ghassemi-Armaki et al. [4,5] reported the incubation time of 3,500~5,000 h at 650°C and ~100,000 h at 600°C in G91. The incubation time for subgrain recovery can be significantly shortened under creep by two additional recovery mechanisms, namely, strain-induced subgrain recovery, and strain-assisted static subgrain recovery. The aging-induced and strain-assisted static recovery mechanisms can result in the breakdown of the creep strength in long-term creep region in G91 [4,5].

The aging-induced subgrain recovery was modeled by considering collective migration of dislocations and boundary suggested by Sandstrom [1,2]. The growth rate of the subgrain width, λ_{sg} is described by the following equation:

$$\frac{d\lambda_{sg}}{dt} = aM\tau/\lambda_{sg} \tag{5}$$

where M is the dislocation mobility, τ is the dislocation line tension, and a is the constant (~5.5). The climb mobility of dislocations was assumed in subgrain recovery [6], and Eq. (5) is rewritten as:

$$\frac{d\lambda_{sg}}{dt} = A\frac{\mu(T)b^3D}{kT}\frac{1}{\lambda_{sg}}$$

$$\lambda_{sg}^2(t) - \lambda_{sg}^2(t=0) = 2A\frac{\mu(T)b^3D}{kT}t \tag{6}$$

where D is the diffusion coefficient, and A is a constant.

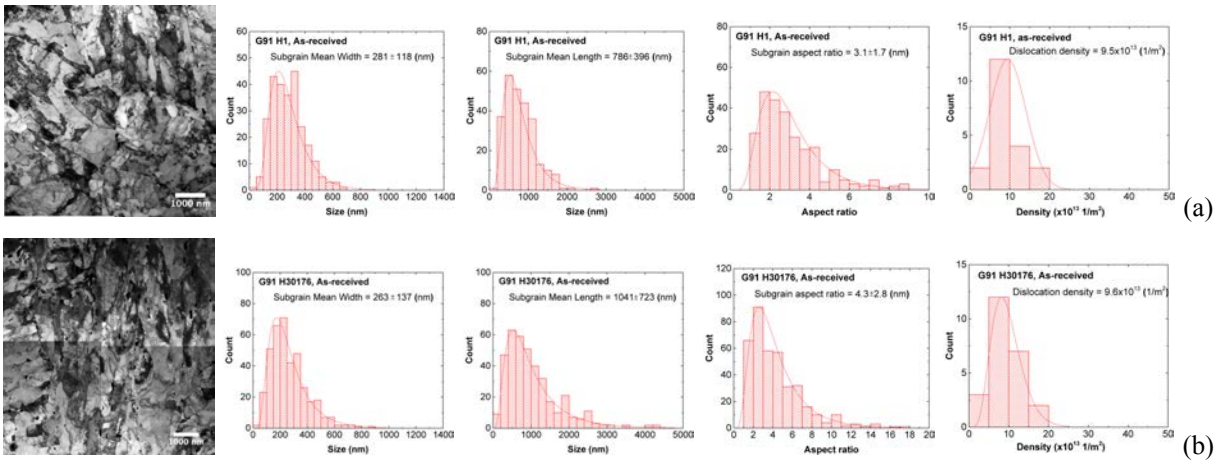

Figure 8. Subgrain structure and distributions of subgrain width, length, and aspect ratio, and dislocation density in the as-received condition in two different heats of G91 (a) G91-H1, and (b) G91-H30176.

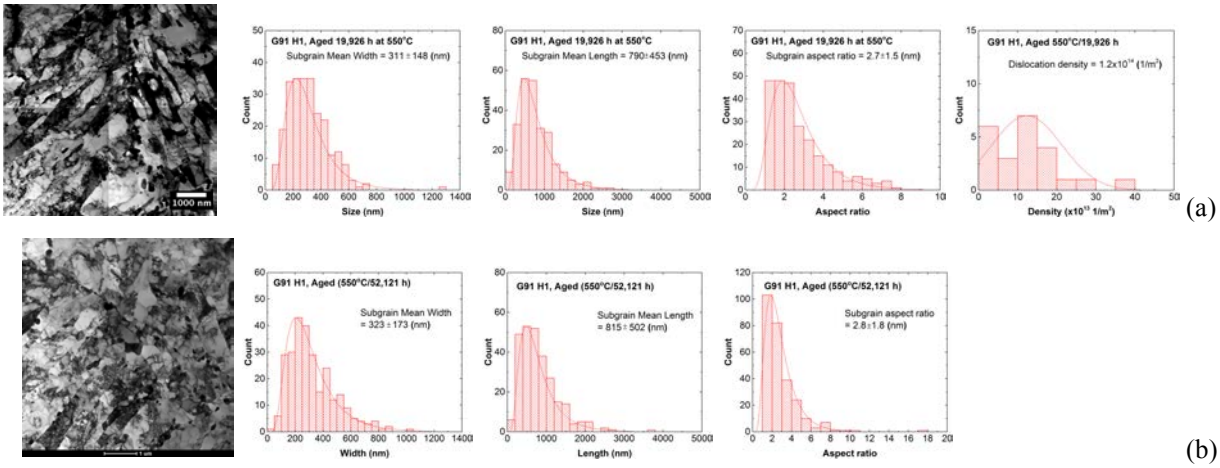

Figure 9. Subgrain structure and distributions of subgrain width, length, and aspect ratio, and dislocation density in G91-H1 after thermal aging at 550°C for (a) 19,926 h and (b) 52,121 h.

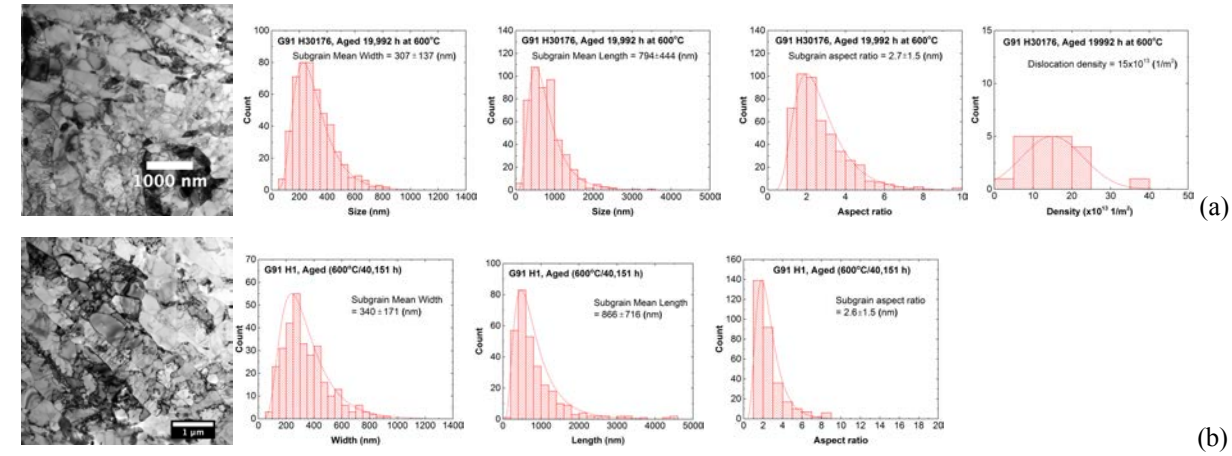

Figure 10. Subgrain structure and distributions of subgrain width, length, and aspect ratio, and dislocation density in (a) G91 H30176 after thermal aging 19,992 h at 600°C, and (b) G91 H1 after thermal aging for 40,151 h at 600°C.

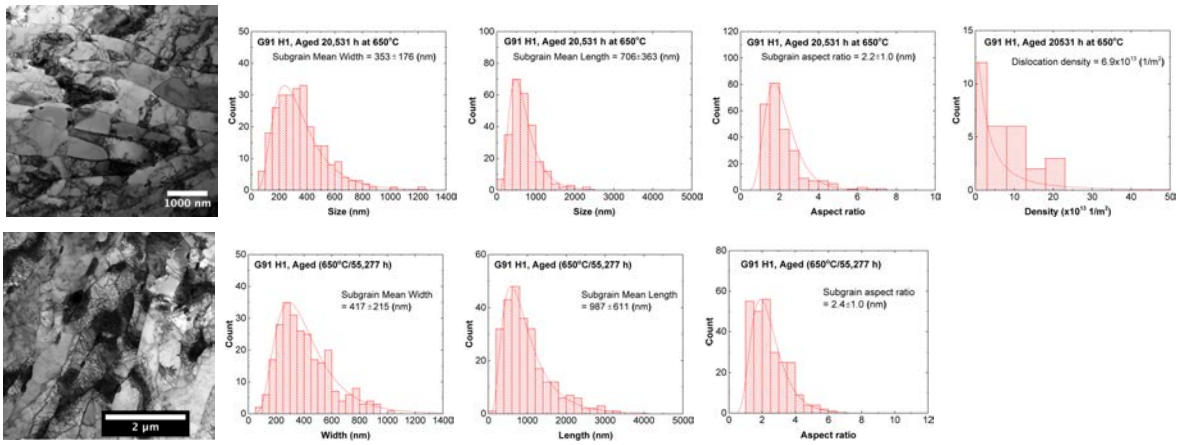

Figure 11. Subgrain structure and distributions of subgrain width, length, and aspect ratio, and dislocation density in G91 H1 after thermal aging at 650°C for (a) for 20,531 h and (b) for 55,277 h.

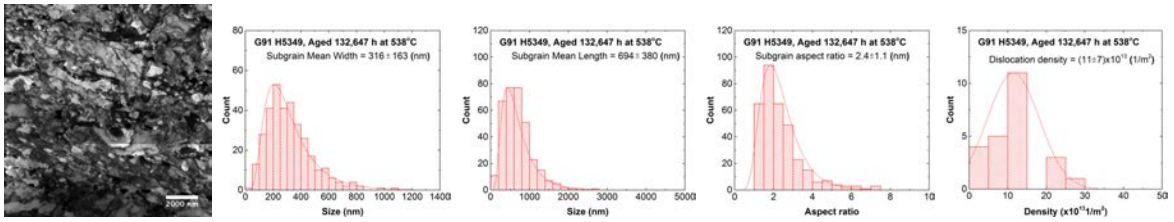

Figure 12. Subgrain structure and distributions of subgrain width, length, and aspect ratio, and dislocation density in G91 H5349 after thermal aging for 132,647 h at 538°C (ID 20842).

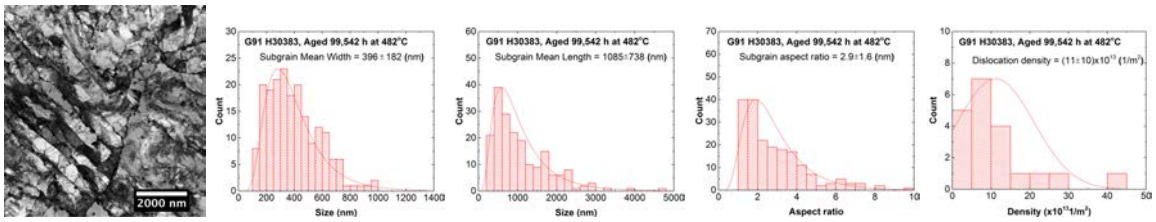

Figure 13. Subgrain structure and distributions of subgrain width, length, and aspect ratio, and dislocation density in G91 H30383 after thermal aging for 99,542 h at 482°C (ID 24746).

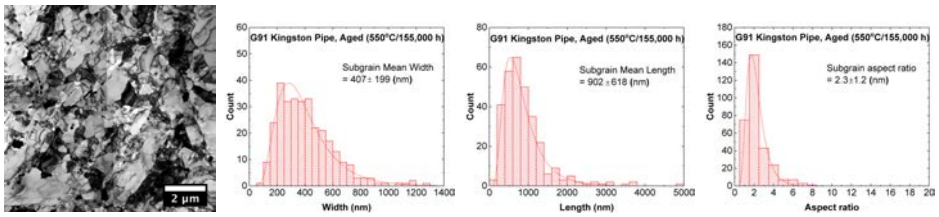

Figure 14. Subgrain structure and distributions of subgrain width, length, and aspect ratio, and dislocation density in G91 Kingston pipe.

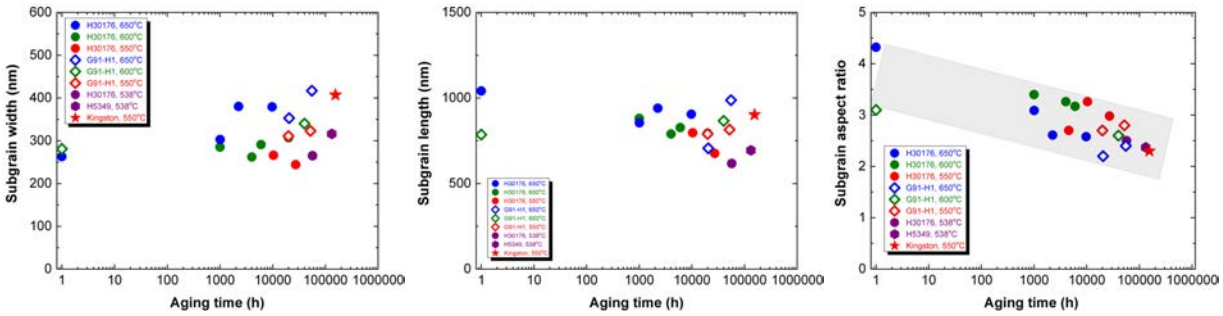

(a) (b) (c)

Figure 15. Time dependence of the subgrain (a) width, (b) length, and (c) aspect ratio of various heats of G91 thermally aged at 538 - 650°C.

The subgrain recovery was modeled using Eq. (6), and the modeling results are compared with the experimental data in Fig. 16 in terms of the subgrain width vs. aging time. While there is a large data scatter in experimental measurements, a general agreement is achieved between the experiments and modeling, and the trends of the subgrain width increase with aging time and temperature can be well captured by the model. The subgrain coarsening was found to be highly sensitive to the aging temperature with an estimated activation energy of 96 kJ/mol.

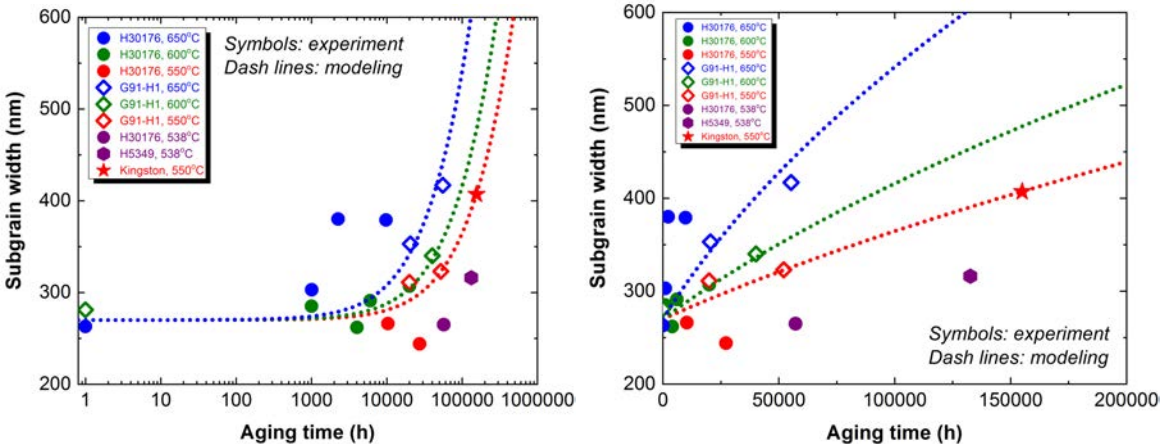

(a) (b)

Figure 16. Comparison of the experimental data and modeling results in terms of the subgrain width vs. aging time for G91 steel (a) linear – log scale and (b) linear – linear scale.

3.1.2 $M_{23}C_6$ carbides

The $M_{23}C_6$ carbides in the normalized and tempered G91 precipitate along grain and subgrain boundaries, and act as obstacles for boundary migration. They are considered as boundary strengtheners, and critical to the stabilization of the tempered martensite structure. However, $M_{23}C_6$ carbides tend to coarsen during thermal aging because of the high solubility of Fe and Cr in the ferrite matrix, and coarsening of $M_{23}C_6$ is detrimental to the high-temperature tensile strength, and creep and creep-fatigue resistance of G91 steel.

Characterization of $M_{23}C_6$ was conducted on the as-received and thermally-aged G91 specimens by TEM and EDS, and the sizes of $M_{23}C_6$ were measured by TEM. Figure 17 shows TEM images of $M_{23}C_6$ particles and particle size distributions in G91-H1 in the as-received condition and after aging at 550°C for 19,926 h and 52,121 h, respectively. Slight particle coarsening was observed at 550°C. A similar observation of $M_{23}C_6$ coarsening was made in G91 specimens aged at 600°C for up to 40,151 h, as shown in Fig. 18 where the $M_{23}C_6$ measurements are shown for G91 H30176 aged at 600°C for 19,992 h and G91-H1 aged at 600°C for 40,151 h. A much more pronounced effect of thermal aging on $M_{23}C_6$ carbide coarsening was observed at 650°C. As shown in Fig. 19, which compares the $M_{23}C_6$ before and after thermal aging at 650°C for 20,531 h and 55,277 h for G91-H1, coarsening of $M_{23}C_6$ particles was much more significant during aging at 650°C than at lower temperatures. The size distributions of $M_{23}C_6$ become broader with some larger sizes of particles formed during aging. Characterization of $M_{23}C_6$ carbides in the Kingston pipe and archived specimens (ID 20842, H5349 aged for 132,647 h at 538°C and ID 24746, H 30383 aged for 99,542 h at 482°C) (Fig. 20) shows a general agreement of $M_{23}C_6$ coarsening as found in G91-H1 and H30176 aged at 550-650°C.

Figure 21(a) summarizes the mean size data of $M_{23}C_6$ carbides in G91 thermally aged at 482-650°C. The initial mean size of $M_{23}C_6$ particles in the normalized and tempered condition shows strong heat dependence. The mean sizes of $M_{23}C_6$ particles vary from 102 in G91-H1 to 134 nm in H30176. The heat variations made it difficult to accurately evaluate the $M_{23}C_6$ coarsening behavior in thermally-aged G91. To further understand the coarsening behavior of $M_{23}C_6$ carbides, computer simulations were carried out using the Thermo-Calc and DICTRA software package. Figures 21 (b), (c) and (d) show the calculated $M_{23}C_6$ size as a function of time at aging temperature, 550, 600, and 650°C, respectively. The interfacial energy was assumed to be 0.1 J/m^2. The simulations show that the coarsening rate of $M_{23}C_6$ particles increases with the aging temperature, and significant coarsening occurs at 650°C, which is consistent with the experimental observations.

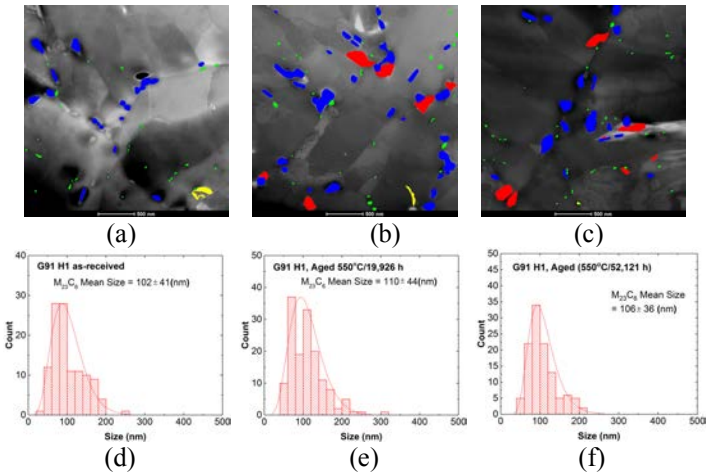

Figure 17. TEM images showing $M_{23}C_6$ carbides (blue), MX precipitates (green and yellow), and Laves phase (red), and $M_{23}C_6$ carbide size distributions in G91-H1: (a) and (d) as-received, (b) and (e) aged (19,926 h/550°C), (c) and (f) aged (52,121 h/550°C).

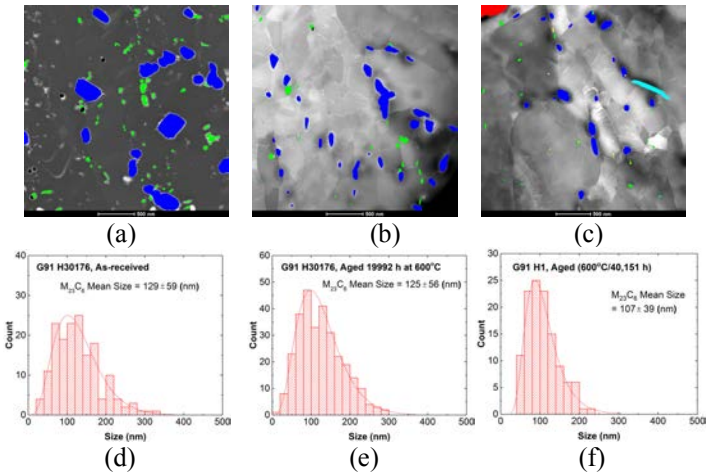

Figure 18. TEM images showing $M_{23}C_6$ carbides (blue), MX precipitates (green and yellow), and Laves phase (red), and $M_{23}C_6$ carbide size distributions in: (a) and (d) G91 H30176 as-received, (b) and (e) G91 H30176 aged (19,992 h/600°C), (c) and (f) G91-H1 aged (40,151 h/600°C).

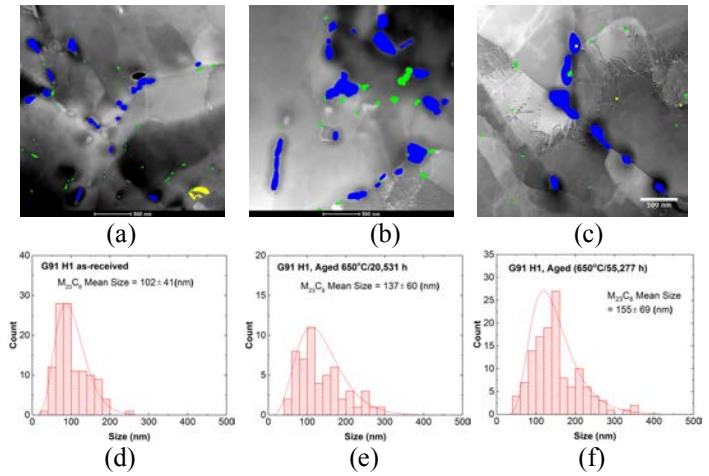

Figure 19. TEM images showing $M_{23}C_6$ carbides (blue), MX precipitates (green and yellow), and Laves phase (red), and $M_{23}C_6$ carbide size distributions in G91-H1: (a) and (d) as-received, (b) and (e) aged (20,531 h/650°C), (c) and (f) aged (55,277 h/650°C).

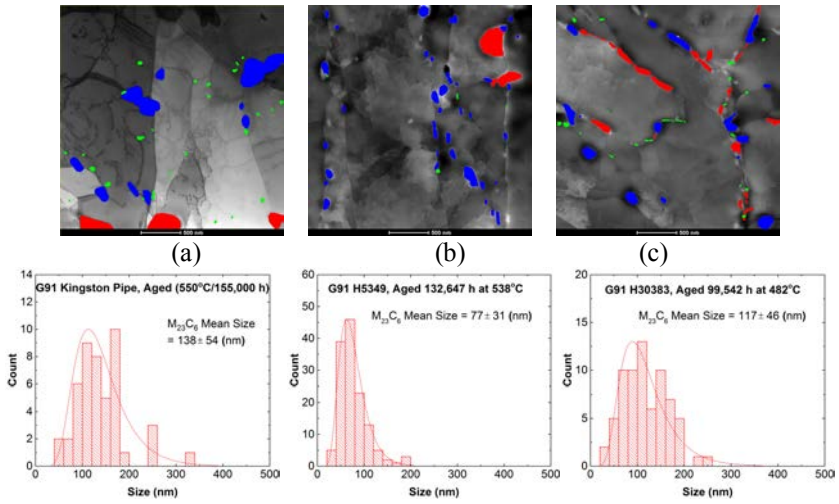

Figure 20. TEM images showing $M_{23}C_6$ carbides (blue), MX precipitates (green and yellow), and Laves phase (red), and $M_{23}C_6$ carbide size distributions for: (a) and (d) G91 Kingston pipe, (b) and (e) G91 H5349 aged (132,647 h/538°C) (ID 20842), (c) and (f) G91 H30383 aged (99,542 h/482°C) (ID 24746).

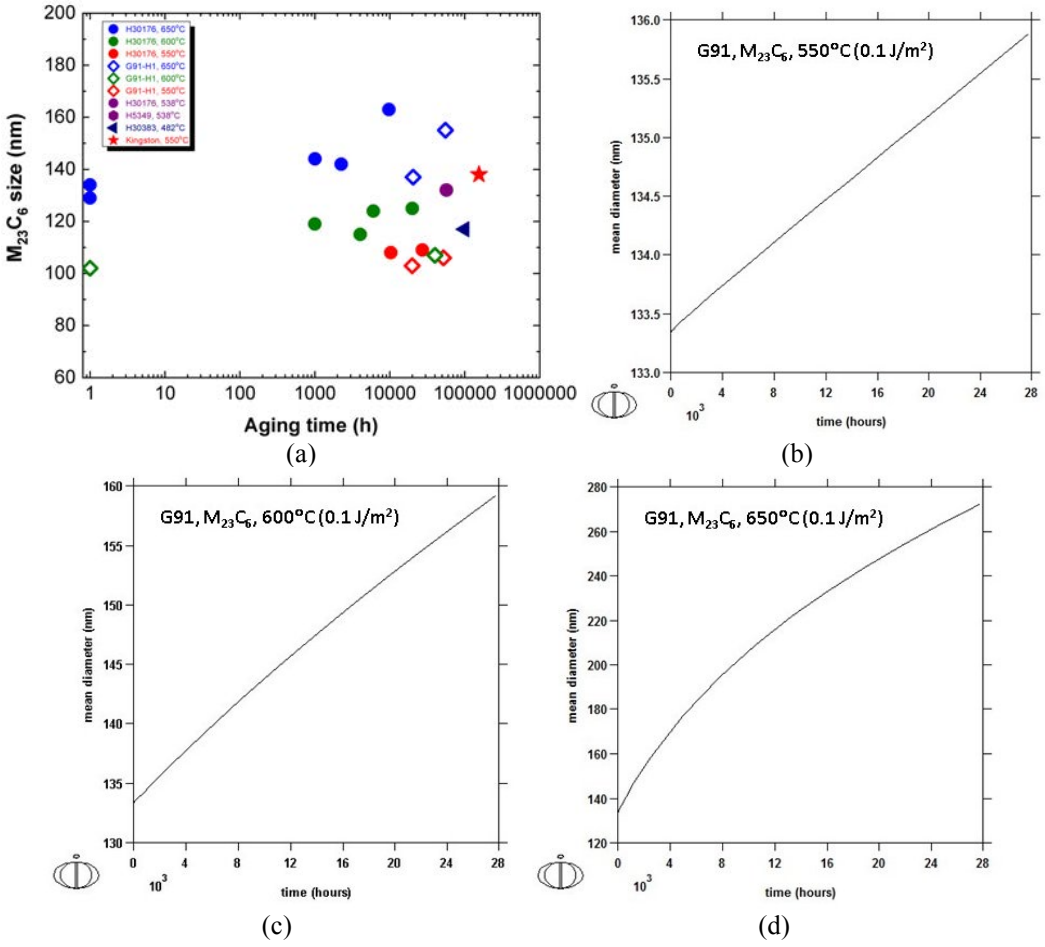

Figure 21. (a) Experimental data of the mean size of $M_{23}C_6$ particles as a function of aging time (b), (c) and (d) the calculated mean size of $M_{23}C_6$ particles as a function of time in G91 aged at 550, 600 and 650°C. The interfacial energy used was 0.1 J/m^2.

3.1.3 MX precipitates

In the normalized and tempered G91, the MX carbonitrides precipitate within subgrains, acting as obstacles to moving dislocations in the matrix and playing an effective role in precipitation strengthening. Since MX carbonitrides are mainly composed of Nb and V and the solubility of Nb and V is small in the ferrite matrix, they do not grow easily during thermal aging.

Detailed analysis of MX precipitates was conducted by TEM on the as-received and thermally-aged G91 specimens. Figure 22 compares the MX in G91-H1 before and after aging at 550°C for 19,926 h and 52,121 h. There are minimal changes in sizes of MX precipitates during aging at 550°C. Thermal aging at 600°C caused minor coarsening of MX precipitates as shown in Fig. 23, where MX measurements for the as-received and 600°C-aged specimens (H30176 aged for 19,992 h/600°C, G91-H1 aged for 40,151 h/600°C) are compared. The effect of thermal aging on MX precipitate sizes is more evident at 650°C. Figure 24 shows the TEM images and size distributions of MX precipitates in G91-H1 before and after aging for 20,531 and 55,277 h at 650°C. Measurements of MX in the archived G91 specimens (ID 20842, H5349 aged for 132,647 h at 538°C) (ID 24746, H 30383 aged for 99,542 h at 482°C), and the Kingston pipe (Fig. 25) revealed a similar coarsening behavior of MX precipitates.

The coarsening behavior of MX precipitates was previously simulated using the thermodynamics and kinetics software package Thermo-Calc and DICTRA, and the results were presented in our earlier reports [7,8]. While the aging-induced MX coarsening behavior was well captured by the simulations, a simple analytical equation is needed to be incorporated into the microstructure – strength model. For this purpose, the classical theory of particle coarsening, so-called the L-S-W theory developed by Lifshitz, Slyozov and Wagner [9,10] was used to model the aging-induced MX coarsening:

$$d^3 - d_0^3 = kt$$
$$k \propto D\gamma X_e \quad (7)$$

where d is the MX mean size (nm) at aging time, t (h), and d_0 is the MX mean size at t = 0, k is the coarsening rate, D is the diffusion coefficient, γ is the interfacial energy, X_e is the equilibrium solubility of large particles. Because both D and X_e increase exponentially with temperature, the coarsening rate, k can be described by an Arrhenius law, i.e.:

$$d^3 - d_0^3 = k' exp(-Q/RT)t \quad (8)$$

where Q is the activation energy, and k' is the constant.

The mean size of MX precipitates as a function of aging time was modeled using Eq. (8), and the modeling results are compared with the experimental data in Fig. 26. While the MX size measurements show a large data scatter and s strong heat dependence, the model in general describes well the coarsening behavior of the MX precipitates. The coarsening rate, k was determined by fitting the experimental data, and the obtained coarsening rate values were used to calculate the activation energy. The estimated activation energy for MX coarsening was 175 kJ/mol, which is equivalent to the activation energy for boundary and core diffusion in α-iron [11].

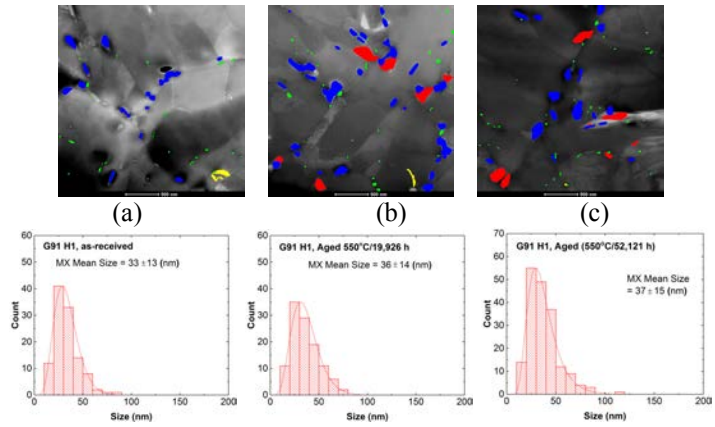

Figure 22. TEM images showing $M_{23}C_6$ carbides (blue), MX precipitates (green and yellow), and Laves phase (red), and MX size distributions for G91-H1: (a) and (d) as-received, (b) and (e) aged (19,926 h/550°C), (c) and (f) aged (52,121 h/550°C).

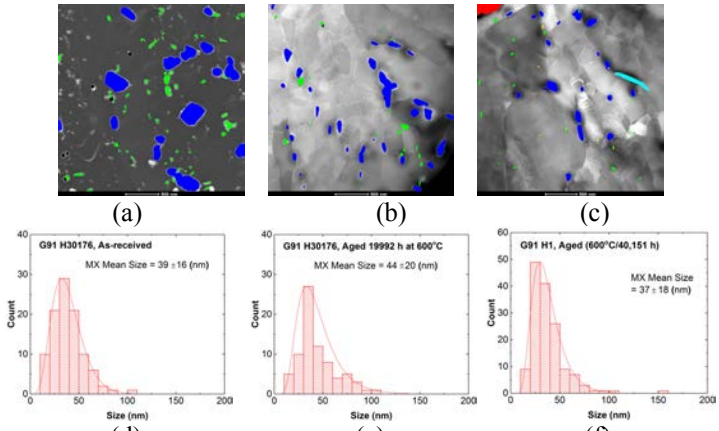

Figure 23. TEM images showing $M_{23}C_6$ carbides (blue), MX precipitates (green and yellow), and Laves phase (red), and MX size distributions for: (a) and (d) G91 H30176 as-received, (b) and (e) G91 H30176 aged (19,992 h/600°C), (c) and (f) G91-H1 aged (40,151 h/600°C).

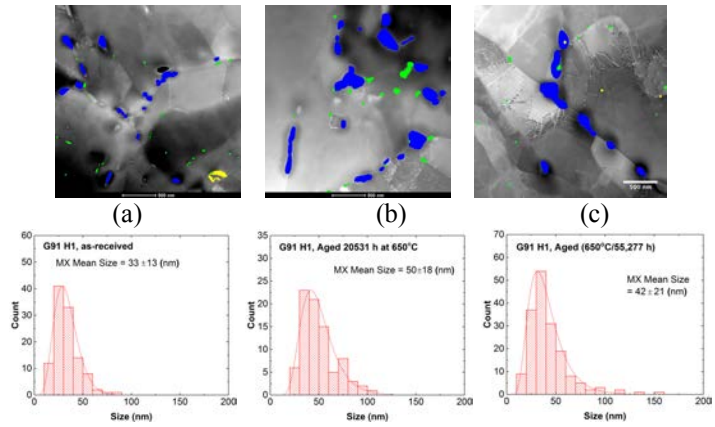

Figure 24. TEM images showing $M_{23}C_6$ carbides (blue), MX precipitates (green and yellow), and Laves phase (red), and MX size distributions for G91-H1: (a) and (d) as-received, (b) and (e) aged (20,531 h/650°C), (c) and (f) aged (55,277 h/650°C).

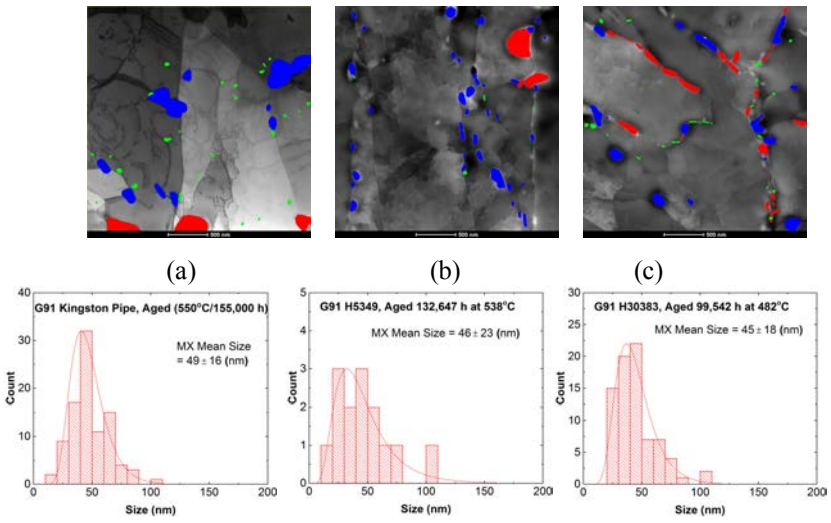

Figure 25. TEM images showing $M_{23}C_6$ carbides (blue), MX precipitates (green and yellow), and Laves phase (red), and MX size distributions for: (a) and (d) G91 Kingston pipe, (b) and (e) G91 H5349 aged for 132,647 h at 538°C (ID 20842), (c) and (f) G91 H30383 aged for 99,542 h at 482°C (ID 24746).

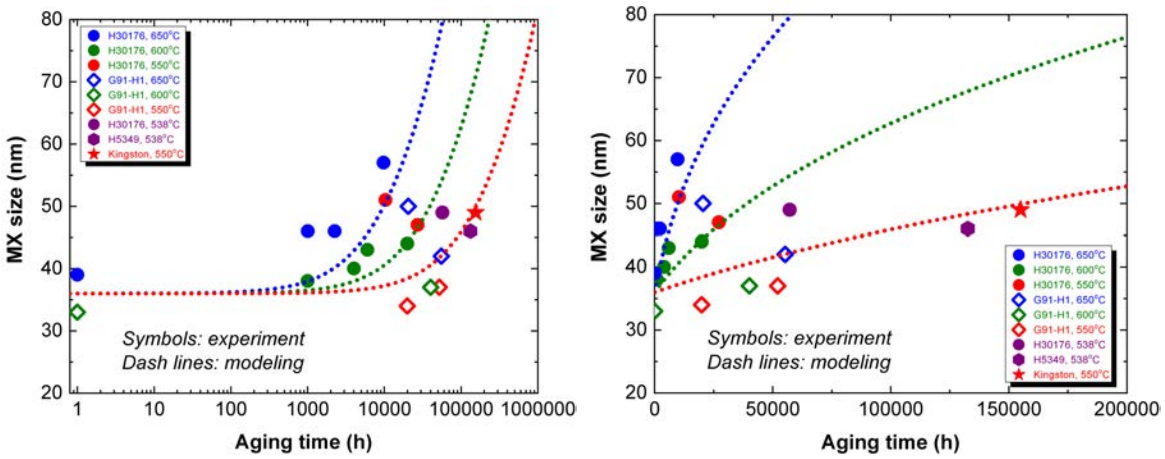

Figure 26. Comparison of the experimental data and modeling results for the mean size of MX vs. aging time for G91 steel (a) linear – log scale and (b) linear – linear scale.

3.1.4 Laves phase

The Laves phase does not exist in the normalized and tempered G91. It forms during thermal aging, as shown in Figs. 17-20, the particles colored in red are the Laves phase formed during thermal aging. The Z-contrast of backscattered electrons (BSE) image and element maps of Mo, Cr, and Fe verify that the Laves phase formed in aged G91 is $(Fe,Cr)_2Mo$. Precipitation of the Laves phase depletes the solid solution strengthener, Mo in the matrix, causing mechanical property degradation in G91. It is noted that a very low number density of AlN (colored in yellow) was observed in the normalized and tempered G91-H1.

Laves phase particles were characterized by both TEM and SEM. The quantitative measurements of Laves phase particles were conducted by SEM using the Z-contrast for statistic reason. Figures 27 – 29 show representative SEM images of Lave phase particles and their size distributions in the G91 specimens thermally aged at 550-650°C and in the Kingston pipe. Thermal aging at 550 and 600°C resulted in the formation of the Laves phase in G91. However, the number density of Laves phase particles in H30176 is significantly lower than that in G91-H1. At 650°C, no Laves phase was observed in Heat 30176 but observed in G91-H1. It is noted that the content of silicon in H30176 is lower than that in G91-H1. Literature shows that silicon plays an important role in the nucleation and growth of the Laves phase in high-Cr ferritic-martensitic steels. Hosoi at al [11] reported that a decrease in Si increases the time required for the formation of the Laves phase, and no Laves phase was detected in ferritic-martensitic steels with negligible Si content. It was suggested that the addition of Si reduces the solubility of Mo in the ferrite phase and promotes the formation of Laves phase [13]. The lower concentration of Si in H30176 is suggested to be responsible for the lower density of the Laves phase precipitates observed in Heat 30176.

Figures 30 (a) and (b) plot the mean size and areal density of Laves phase particles as a function of aging time for various heats of G91 aged at 538 - 650°C. Laves phase particles grow rapidly once they are nucleated, to a few hundreds of nanometers, after aging for a few thousands hours, and then coarsen slowly. The density of Laves phase particles in G91-H1 is significantly higher than that in H30176, and the growth period is significantly longer in H30176 than in G91-H1.

Formation of the Laves phase during thermal aging removes the Mo solute atoms from the matrix, diminishing the solid solution strengthening. The understanding of the Laves phase precipitation behavior is important to the prediction of the long-term performance of G91. The nucleation, growth and coarsening processes of the Laves phase in G91 were simulated using thermodynamics and kinetics software package, Thermo-Calc. Both the simulations and experiments showed that the Laves phase grew rapidly to a size of hundreds of nanometers. Experiments also showed that the Laves phase particles are distributed primarily along grain and subgrain boundaries. The Laves phase particles formed during aging may provide a pinning force on the boundaries but play a minimal role in strengthening in thermally-aged G91. Only the solid solution hardening of Mo solutes may be considered in thermally-aged G91. To estimate the Mo solute strengthening effect in thermally-aged G91, the equilibrium concentration of Mo in the ferrite matrix was calculated by Thermo-Calc, and the values are given in Table 5.

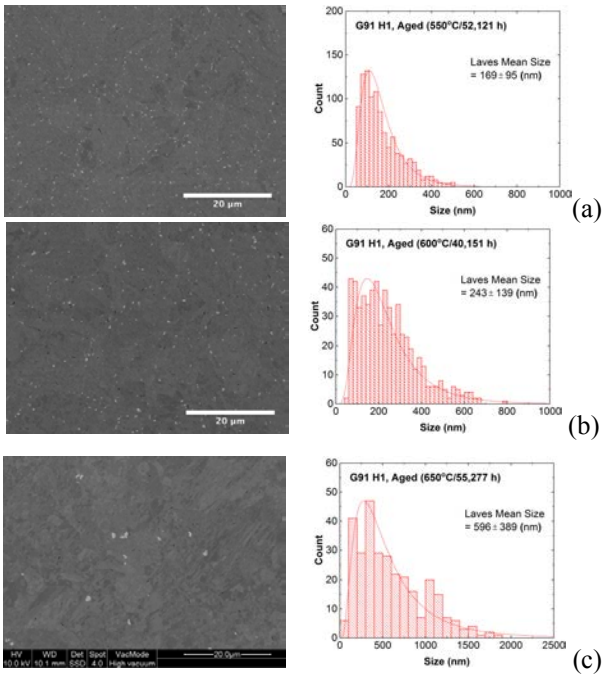

Figure 27. SEM image showing Laves phase and its size distributions in G91-H1 after thermal aging for (a) 52,121 h at 550°C, (a) 40,151 h at 600°C, and (c) 55,271 h at 650°C.

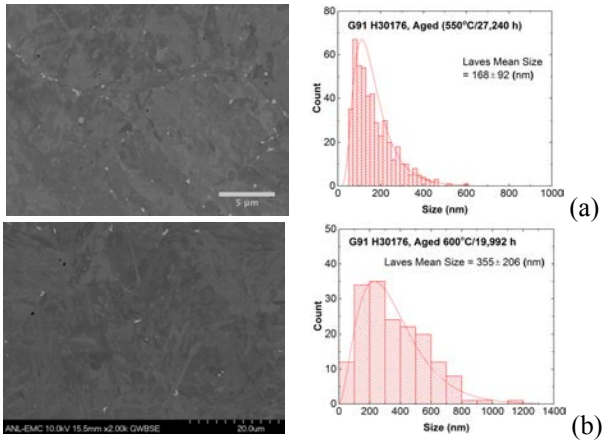

Figure 28. SEM image showing Laves phase and its size distributions in G91-H30176 after thermal aging for (a) 27,240 h at 550°C, (b) 19,992 h at 600°C.

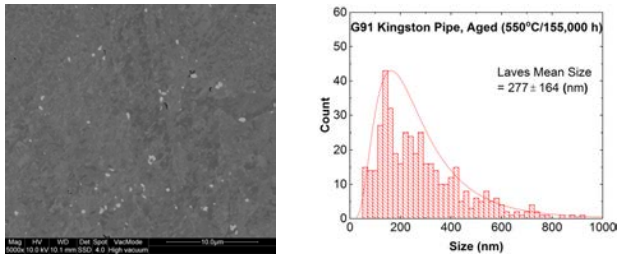

Figure 29. SEM image showing Laves phase, and its size distribution in G91 Kingston pipe.

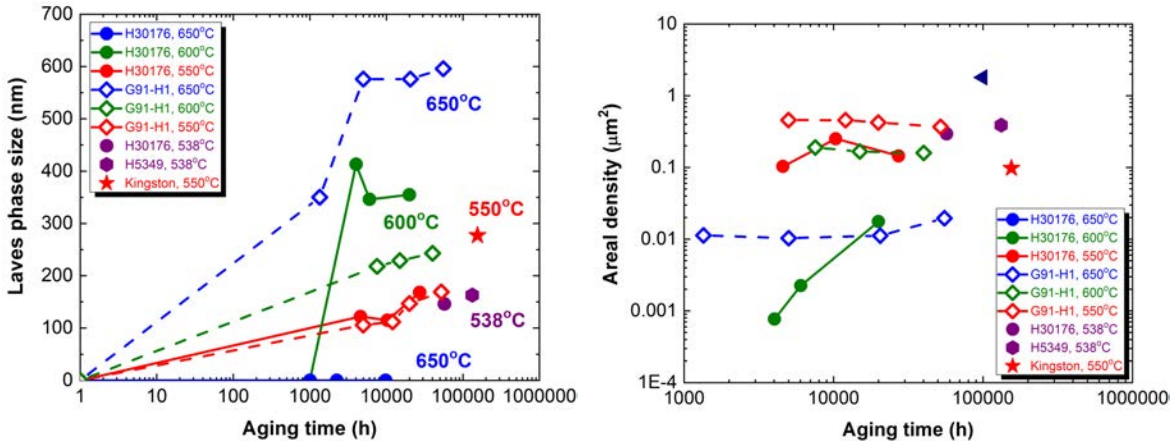

(a) (b)

Figure 30. Time dependence of (a) the mean size and (b) the areal density of Laves phase precipitates in G91 during thermal aging at 550- 650°C.

Table 5. The equilibrium Mo concentration (at%) in the ferrite in G91.

Temperature (°C)	550	600	650
C_{Mo}^{equ} (at%)	0.111	0.229	0.395

3.2 Effect of thermal aging on tensile properties

The stress-strain behavior of the normalized and tempered (N&T) G91 shows strong temperature dependence. Figure 31 shows the engineering stress-strain curves of two heats of G91, H30176 and G91-H1 in the N&T condition that were tensile tested at temperatures of 20 - 650°C at a nominal strain rate of 0.001 s^{-1}. The tensile strength of G91 decreases and the tensile ductility increases with increasing test temperature, except at 400°C where the ductility is the lowest. The strain hardening capability of G91 is nearly lost when it is tested at temperatures of 550°C and above.

To understand the effect of thermal aging on tensile properties of G91, tensile tests of the thermally-aged specimens were carried out at the aging temperature. Figures 32-34 show the yield stress, ultimate tensile strength, uniform elongation, and total elongation as a function of aging time for H30176 and G91-H1 thermally aged at 550, 600, and 650°C, respectively. Thermal aging of G91 resulted in the reduction in the yield stress and the ultimate tensile strength but has an insignificant effect on the uniform and total elongations. The reduction in tensile strength is more pronounced as the aging temperature and time increases. The two heats of G91 perform similarly under thermal aging at 550 - 650°C.

Tensile specimens made from the archived crept G91 specimens were tested at the aging temperature as well, and the yield stress, the ultimate tensile strength, the uniform elongation, and the total elongation of the 13 archived specimens and the specimen made from the G91 Kingston tube are compared in Figs. 35 (a) – (d). Specimens of H30176 were used as control specimens for all the heats. The micro-hardness values of the archived specimens are given in Fig. 32(e). The hardness values can be correlated with the tensile strength at room temperature. While no clear trend can be observed from the hardness data, the ultimate tensile strength indeed exhibits a slight decrease after long-term thermal aging at temperatures > 500°C. The total elongation remains adequate after >100,000 h aging above 500°C.

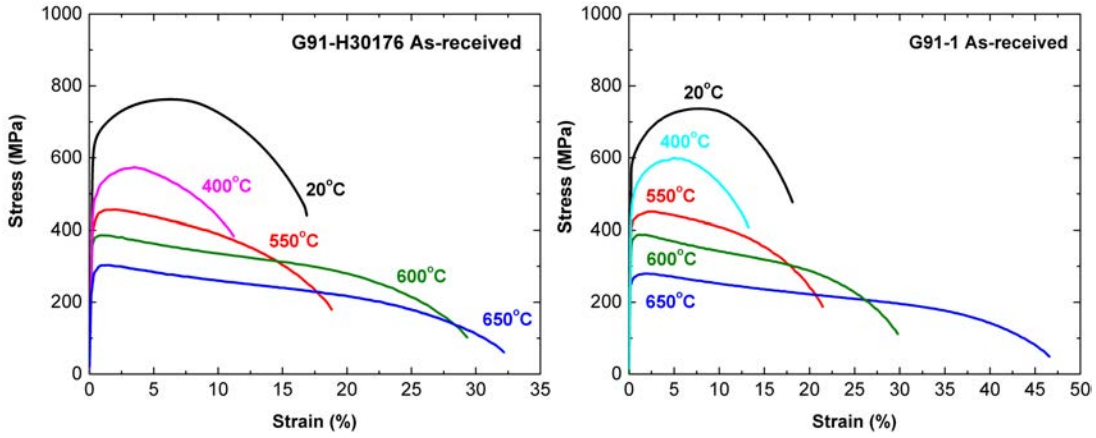

(a) (b)

Figure 31. Stress-strain curves of the as-received G91 (a) Heat 30176 and (b) Heat G91-H1.

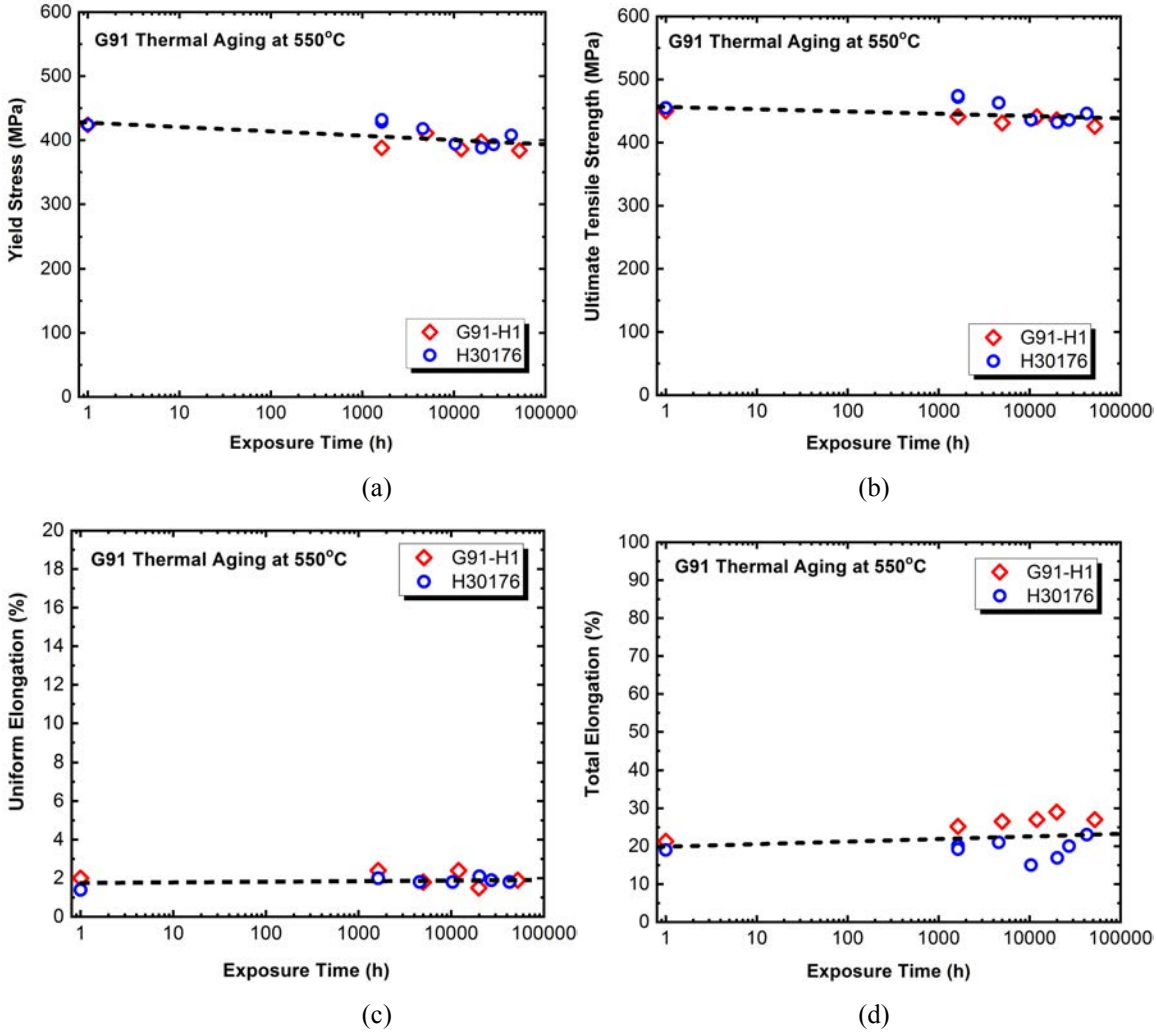

(a) (b)

(c) (d)

Figure 32. The (a) yield stress, (b) ultimate tensile strength, (c) uniform elongation, and (d) total elongation as a function of aging time for G91-H1 and H30176 thermally aged at 550°C.

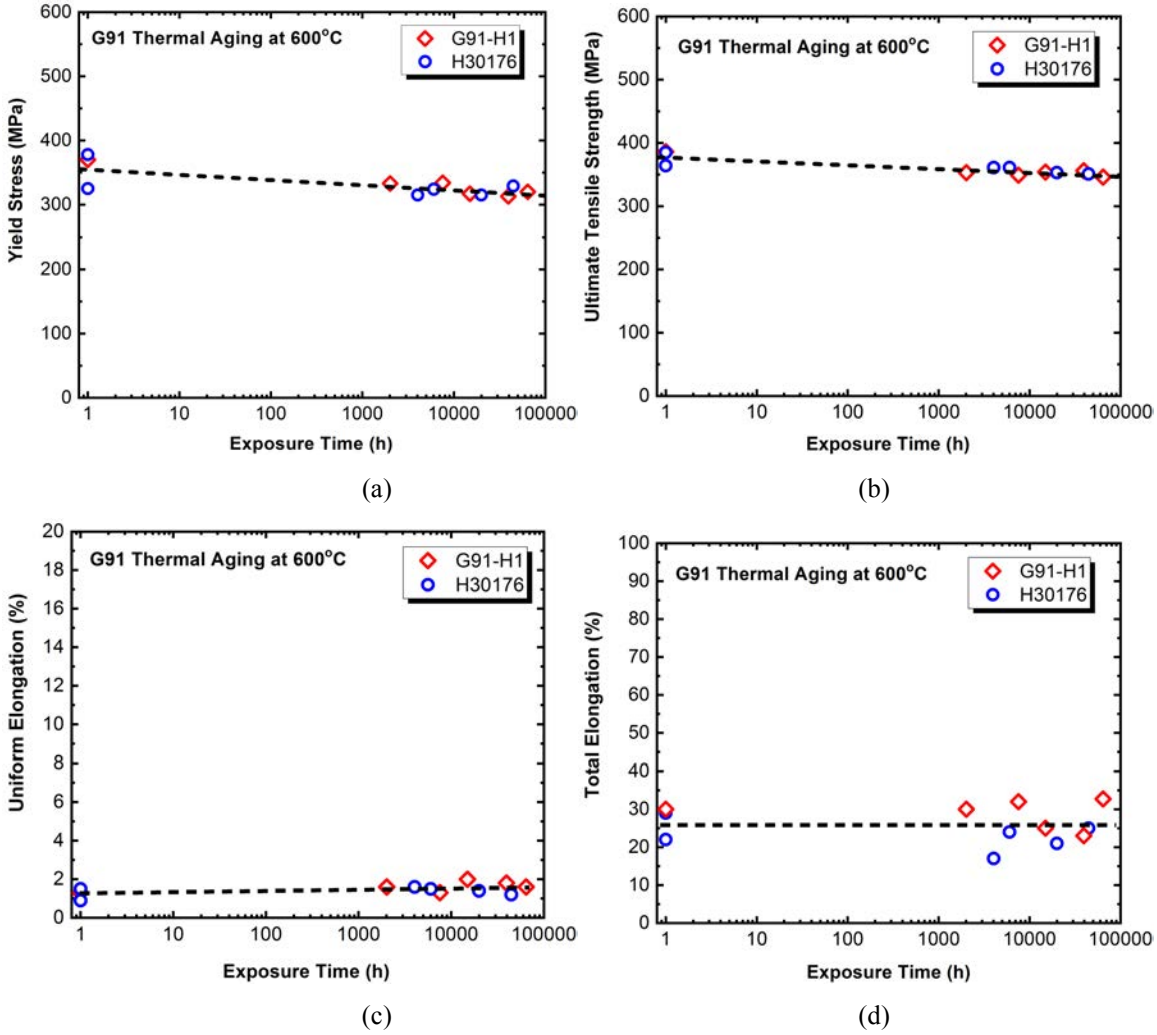

Figure 33. The (a) yield stress, (b) ultimate tensile strength, (c) uniform elongation, and (d) total elongation as a function of aging time for G91-H1 and H30176 thermally aged at 600°C.

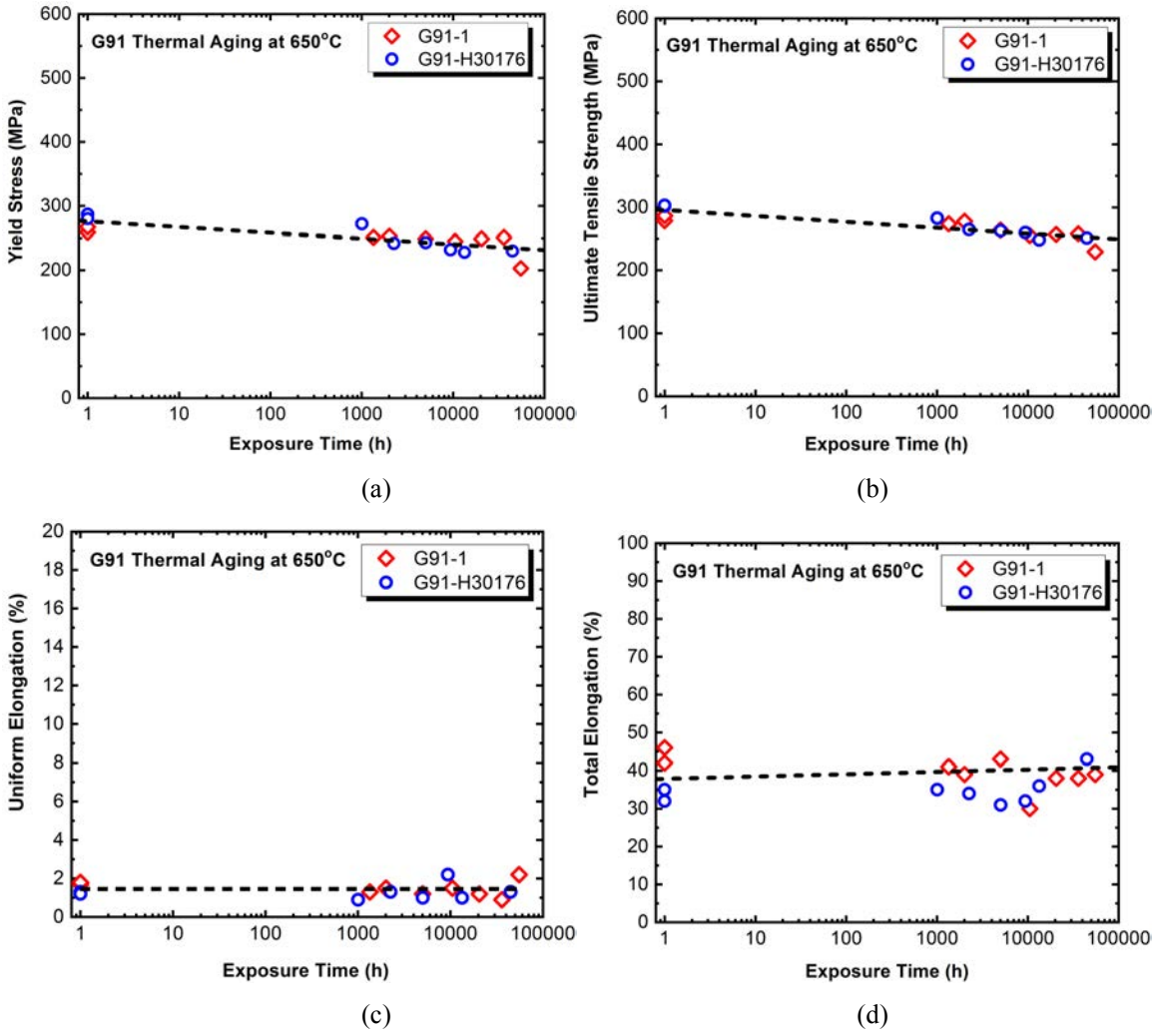

Figure 34. The (a) yield stress, (b) ultimate tensile strength, (c) uniform elongation, and (d) total elongation as a function of aging time for G91-H1 and H30176 thermally aged at 650°C.

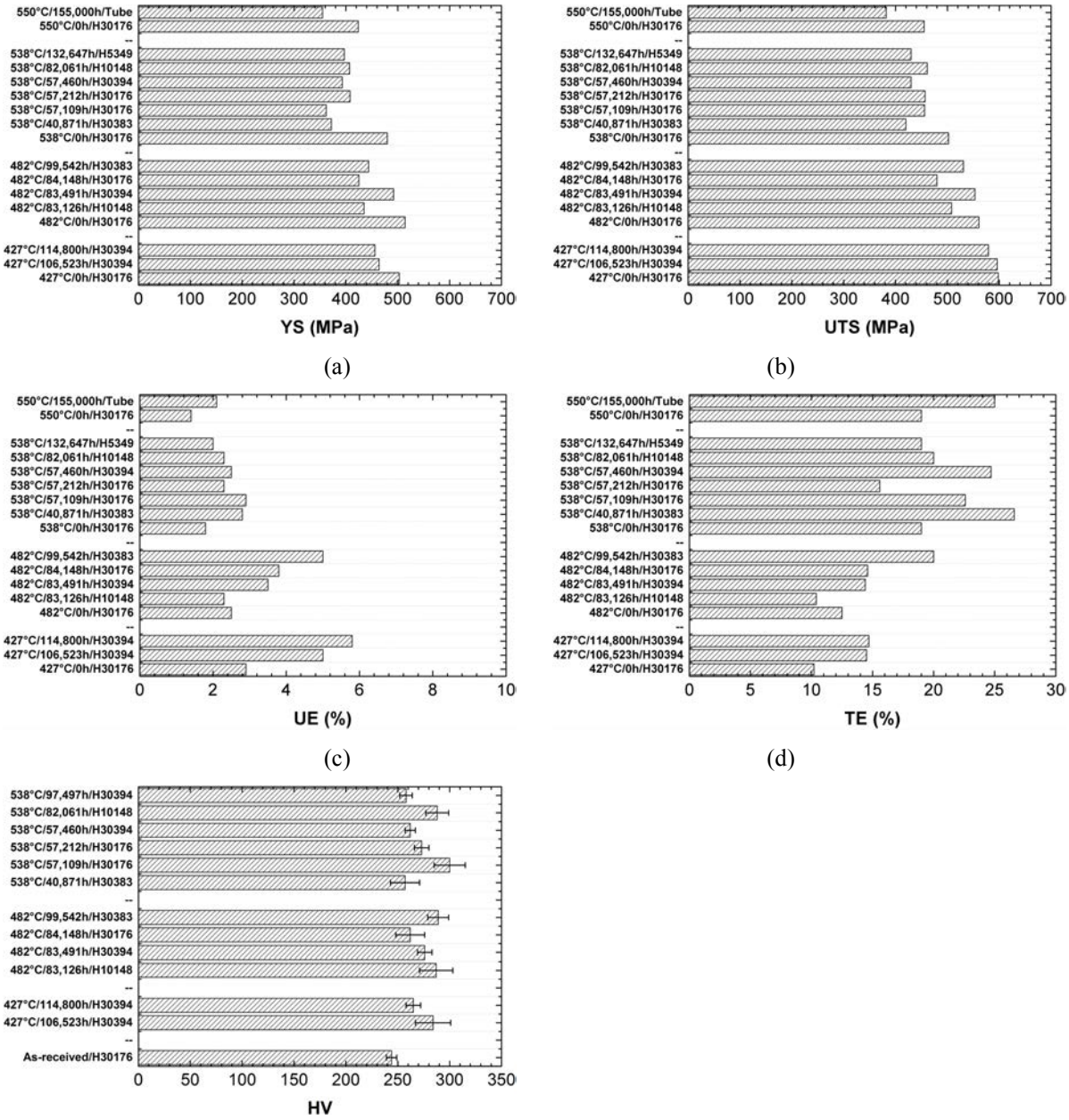

Figure 35. The (a) yield stress, (b) ultimate tensile strength, (c) uniform elongation, (d) total elongation, and (e) micro-hardness for the archived G91 specimens thermally-aged at 427 - 550°C. The tensile test was conducted at the aging temperature.

3.3 Correlation of microstructure - tensile strength

3.3.1 Strengthening mechanisms

The yield stress (YS) and ultimate tensile strength (UTS) data of various heats of G91 thermally-aged at 427 - 650°C are summarized in Fig. 36. All the tensile tests were conducted at the aging temperature. There are clear trends of reductions in the YS and UTS with increasing aging temperature and time. As the aging temperature increases, the reductions in YS and UTS occur at a shorter time, and the strength reductions are more significant at higher temperatures.

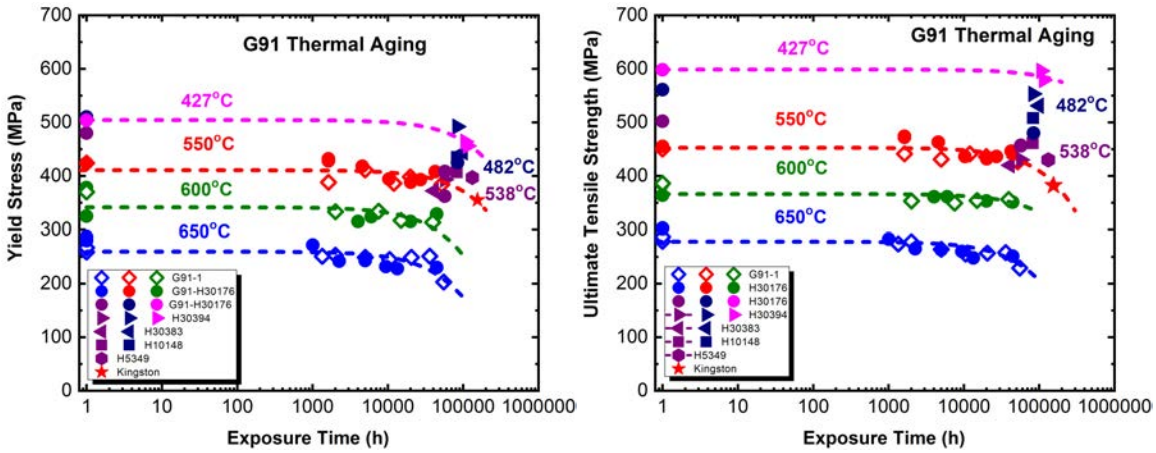

(a) (b)

Figure 36. Experimental data showing the effects of thermal aging on (a) the yield stress and (b) ultimate tensile strength of G91. Lines are a guide for the eye.

Efforts were made to understand the strengthening mechanisms and degradation processes and their correlation with microstructural evolution during long-term aging. Before aging, the microstructure of G91 consists of tempered martensite with a high density of dislocations; grain and subgrain boundaries are decorated with $M_{23}C_6$ carbides; vanadium/niobium carbonitrides (MX) are uniformly distributed within subgrains. As reported in the previous section, thermal aging causes significant microstructural changes including a decrease in dislocation density within subgrains, subgrain recovery, coarsening of $M_{23}C_6$ and MX precipitates, and the formation of a new phase, the Laves phase. These microstructural changes occur in a coupled way. For instance, the dispersion of $M_{23}C_6$ particles along boundaries exerts the pinning force on subgrain boundaries, which hinders subgrain coarsening and growth. The slower the particle coarsening rate the longer is the time before unpinning of the subgrain boundaries and consequent secondary recrystallization and martensite grain growth. Ghassemi-Armaki et al. [4,5] reported a good correlation of subgrain width with $M_{23}C_6$ particle spacing. The MX precipitates in the matrix play a different role, serving as effective obstacles to moving dislocations and giving rise to precipitation strengthening in G91. Because of the effect of MX particles on dislocation motion, it also affects the recovery rate of subgrains, but to a much less extent compared to $M_{23}C_6$ carbides. While the formation of the Laves phase removes the solute strengthener, Mo from the matrix, reducing solid solution strengthening in G91, the Laves phase particles precipitate along grain boundaries and sub-boundaries, which

also affect subgrain recovery. The interactive processes of these microstructural constituents collectively contribute to the recovery of the microstructure, transforming it to a more stable structure and reducing the excessive energy stored in the initial metastable structure.

To understand the precise role of each microstructural constituent and their quantitative contributions to the yield and tensile strength of G91 steel, *in situ* tensile tests with high-energy synchrotron X-rays were conducted on the as-received G91 at 20 - 650°C at beamline 1-ID at the Advanced Photon Source, and the results were reported in [14,15]. To summarize, we have found that there is a significant load transfer from the martensite matrix to $M_{23}C_6$ and MX phases during tensile deformation at 20°C. The $M_{23}C_6$ particles showed a much greater load sharing capability than MX precipitates. The load transfer was significantly reduced at higher temperatures, and became minimal at 650°C. The *in situ* tensile tests also revealed that the role of $M_{23}C_6$ carbides in the strengthening of G91 must be understood by taking into account of their non-uniform distribution in the martensite matrix. The primary role of $M_{23}C_6$ carbides is to provide a pinning force on grain and subgrain boundaries, hindering their coarsening and growth. The coarsening of $M_{23}C_6$ carbides will reduce the boundary pinning effects, leading to a loss of strength. The strengthening effect of $M_{23}C_6$ particles measured by synchrotron X-rays manifested subgrain boundary strengthening in G91. The high loading capacity of $M_{23}C_6$ particles measured by the lattice strain was consistent with the dislocation activity in the matrix revealed by the X-ray line profile analysis, and sub-boundary strengthening in G91 was the dominant hardening mechanism in G91. This finding agrees with the observations reported in other studies [16,17] that sub-boundary hardening is much greater than precipitate hardening of MX and the Laves phase particles in high-Cr ferritic-martensitic steels.

3.3.2 Microstructure - strength model for thermally-aged G91

The strength of G91, σ can be expressed as a function of the following microstructural parameters:

$$\sigma = f(c, \rho, \lambda_{sg}, \lambda^{i}_{par}) \quad (9)$$

where c is the Mo solid solution content, ρ is the dislocation density within subgrains, λ_{sg} is the subgrain width, and λ^{i}_{par} is the particle spacing of second phase i. This relationship considers several strengthening mechanisms including solid solution strengthening, dislocation hardening, sub-boundary strengthening, and precipitation hardening. From the understanding of G91 microstructure and the *in situ* tensile test measurements, we propose that the tensile strength of G91 is accounted for by three superimposed strengthening effects: subgrain boundary hardening, MX precipitation hardening, and Mo solid solution strengthening, namely:

$$\sigma = \sigma_{fer} + \sigma_{ss} + \sigma_{sg} + \sigma_{MX} \quad (10)$$

where σ_{fer} is the strength of a fully-annealed Fe-9Cr model alloy with the grain size comparable to G91 (~20 μm), σ_{ss} is the strength component associated with Mo solid solution strengthening, σ_{sg} is the subgrain boundary strengthening contribution, and σ_{MX} is associated with MX precipitation hardening. Because of interactive effects on subgrain recovery from $M_{23}C_6$ carbides and Laves phase particles distributed along the boundaries and dislocations within subgrains, the role of $M_{23}C_6$ carbides, Laves phase and dislocations on the tensile strength was described by the subgrain

boundary hardening. We have also made an assumption that thermal aging affects all the strength components except σ_{fer}.

The Mo solid solution strengthening in the matrix can be estimated by [18]:

$$\sigma_{ss} = \alpha_{ss}\mu(T)\varepsilon^{1.5}c^{0.5} \quad (11)$$

where ε is the misfit strain, c is the Mo solute concentration (at%), and α_{ss} is the constant. The misfit strain was estimated to be ~1.3 [19]. In the as-received G91, assuming all the Mo (0.6 at%) is in the solution, the Mo solid solution strengthening effect is estimated to be 9-10 MPa at 550-650°C, which is a small fraction of the total strength. Due to the formation of the Laves phase under aging, the Mo solutes will be depleted from the matrix, reducing the solid solution strengthening effect. Because of the small effect of the Mo solute strengthening, the value of σ_{ss} for thermally-aged G91 was calculated using the Mo equilibrium concentrations given in Table 5, and the time dependence was neglected.

The contribution of subgrain boundary hardening to the tensile strength of G91, σ_{sg} can be estimated using the following equation [20]:

$$\sigma_{sg} = \frac{MK\mu(T)b}{\lambda_{sg}} \quad (12)$$

where λ_{sg} is the subgrain width, μ is the shear modulus, b is the Burger's vector (0.248 nm), M is the Taylor factor, and K is the constant. To take into account of the thermally-activated process of plastic deformation at high temperature, Eq. (12) was modified to include the grain size-dependent dislocation creep [21], and rewritten as:

$$\sigma_{sg} = MK'exp(\frac{Q_B}{mRT})\mu(T)b \cdot \lambda_{sg}^{-1} \quad (13)$$

where Q_B is the activation energy for grain boundary diffusion, and K' and m are the constants. The subgrain width was calculated by Eq. (6), and the value of σ_{sg} for thermally-aged G91 was evaluated using Eq. (13).

The MX precipitation hardening, σ_{MX} can be described by the Orowan mechanism [22]:

$$\sigma_{MX} = M \cdot \sqrt{6f/\pi} \cdot \mu(T)b/\lambda_{MX}$$

$$\lambda_{MX} = 0.277 d_{MX}(4\pi/3f)^{1/3} \quad (14)$$

where λ_{MX} is the MX inter-particle spacing, d_{MX} is the MX particle diameter, f is the MX volume fraction, and M is the Taylor factor. The MX size was calculated by Eq. (8), and the MX precipitation strengthening in thermally-aged G91 was calculated by Eq.((14). It should be noted that the model does not take into account of the formation of Z-phase, which will replace the MX precipitates after long-term aging based on the Thermo-Calc prediction. In the thermally-aged G91 specimens examined so far, no Z-phase precipitates have been observed. The volume fraction of MX calculated by Thermo-Calc was used in the strength calculations, which is 0.004 at 550-650°C.

The strength of a fully-annealed Fe-9Cr model alloy with the grain size comparable to G91 (~20 μm), σ_{fer} was estimated as follows: according to Codd and Petch [23], the lower yield stress of iron with the grain size of ~20 μm is ~210 MPa at room temperature. According to Frost and

Ashby [11], the shear stress of pure iron of grain size 100 μm is about 0.001μ (550°C), 0.00095μ (600°C), and 0.00075μ (650°C), respectively. The values of σ_{fer} were estimated to be 186, 168, and 124 MPa at 550, 600, and 650°C. The temperature dependence of the shear modulus of G91 was taken from [24]. The value of σ_{fer} represents the minimum strength of thermally-aged G91 at which it completely loses the subgrain boundary hardening and the precipitation strengthening.

The calculated YS – aging time and UTS – aging time curves for thermally-aged G91 are shown in Fig. 37. The experimental data obtained in this study are included to compare the claculations. An excellent agreement was achieved between the experiments and the calculations for aging time up to ~150,000 h. The calculations show that sub-boundary strengthening becomes weaker at high temperature, and the activation energy was estimated to be 31 kJ/mol, ~$Q_B/6$. An activation energy of $Q_B/8$ was suggested in the Blum-Zeng model to account for grain size-dependent dislocation creep [25].

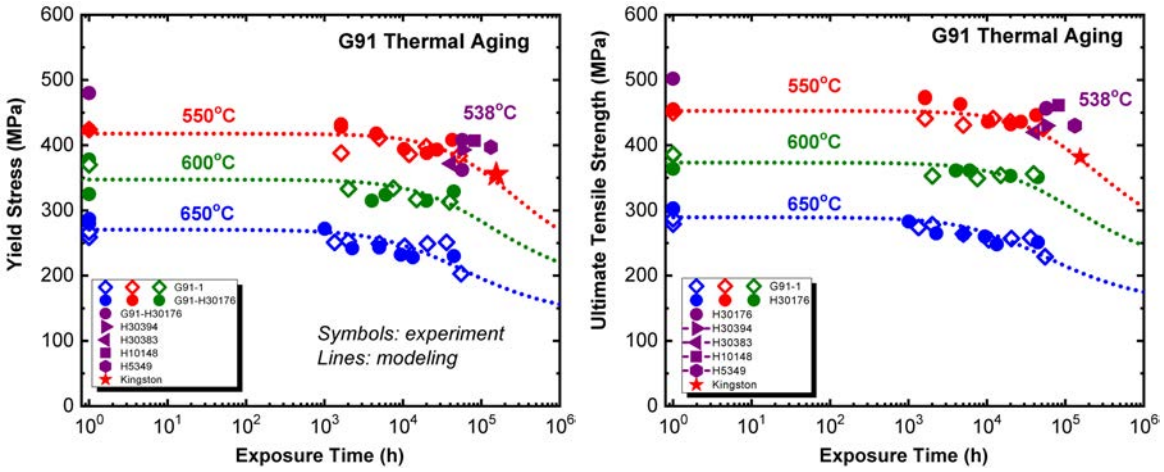

(a) (b)

Figure 37. Comparison of the calculated (a) yield and (b) tensile strength using the microstructure-strength model and the experimental data for G91 aged at 550-650°C.

3.3.3 Predicted Thermal Aging Strength Reduction Factors

The ASME B&PV Code Section III, Subsection NH (new Division 5) provides the yield and tensile strength reduction factors for G91 due to long term elevated temperature service. The yield strength reduction factor is 1 (Table NH-3225-2), and the tensile strength reduction factor is given Table NH-3225-4. We calculated the yield and tensile strength reduction factors for thermally-aged G91 using the microstructure – strength model presented in the previous section. The predicted tensile and yield strength reduction factors and the ASME Code values are summarized in Tables 6 and 7, respectively. The numbers in *italic and red* are the predicted values. Table NH-3225-4 provides the tensile strength reduction factors for times up to 3×10^5 h (34 yr). We calculated the yield and tensile strength reduction factors for times up to 1×10^6 h (114 yr). The predicted values are generally lower than the ASME Code numbers, and the differences become more significant as time and temperature increase. According to the predictions, G91 can retain

70% of its initial yield strength and 72% of tensile strength at the end life of 1×10^6 h at the operating temperature of 500°C.

Table 6 Tensile strength reduction factors – ASME Table NH-3225-4 and predicted values (shown in italic and red).

	1 (h)	10 (h)	3×10^1 (h)	1×10^2 (h)	3×10^2 (h)	1×10^3 (h)	3×10^3 (h)	1×10^4 (h)	3×10^4 (h)	1×10^5 (h)	3×10^5 (h)	5×10^5 (h)	1×10^6 (h)
500°C	1	1	1	1	1	1	1	1	1	0.97	0.97	NA	NA
	1	*1*	*1*	*1*	*1*	*1*	*1*	*0.99*	*0.97*	*0.93*	*0.84*	*0.79*	*0.72*
525°C	1	1	1	1	1	1	1	1	1	0.94	0.91	NA	NA
	1	*1*	*1*	*1*	*1*	*1*	*1*	*0.99*	*0.96*	*0.90*	*0.81*	*0.76*	*0.69*
550°C	1	1	1	1	1	1	1	1	0.94	0.92	0.89	NA	NA
	1	*1*	*1*	*1*	*1*	*1*	*0.99*	*0.98*	*0.95*	*0.87*	*0.78*	*0.73*	*0.67*
575°C	1	1	1	1	1	1	1	0.95	0.92	0.88	0.83	NA	NA
	1	*1*	*1*	*1*	*1*	*1*	*0.99*	*0.97*	*0.93*	*0.85*	*0.75*	*0.71*	*0.67*
600°C	1	1	1	1	1	1	0.96	0.92	0.89	0.85	0.84	NA	NA
	1	*1*	*1*	*1*	*1*	*1*	*0.99*	*0.97*	*0.92*	*0.83*	*0.74*	*0.70*	*0.66*
625°C	1	1	1	1	1	0.97	0.94	0.90	0.87	0.83	0.81	NA	NA
	1	*1*	*1*	*1*	*1*	*0.99*	*0.98*	*0.95*	*0.88*	*0.79*	*0.70*	*0.67*	*0.64*
650°C	1	1	1	1	0.98	0.94	0.91	0.87	0.84	0.81	0.78	NA	NA
	1	*1*	*1*	*1*	*1*	*0.99*	*0.97*	*0.92*	*0.84*	*0.74*	*0.66*	*0.64*	*0.60*

Table 7 Yield strength reduction factors – ASME Table NH-3225-2 and predicted values (shown in italic and red).

	1 (h)	10 (h)	3×10^1 (h)	1×10^2 (h)	3×10^2 (h)	1×10^3 (h)	3×10^3 (h)	1×10^4 (h)	3×10^4 (h)	1×10^5 (h)	3×10^5 (h)	5×10^5 (h)	1×10^6 (h)
500°C	1	1	1	1	1	1	1	1	1	1	1	NA	NA
	1	*1*	*1*	*1*	*1*	*1*	*1*	*0.99*	*0.97*	*0.92*	*0.83*	*0.77*	*0.70*
525°C	1	1	1	1	1	1	1	1	1	1	1	NA	NA
	1	*1*	*1*	*1*	*1*	*1*	*1*	*0.99*	*0.96*	*0.90*	*0.79*	*0.74*	*0.67*
550°C	1	1	1	1	1	1	1	1	1	1	1	NA	NA
	1	*1*	*1*	*1*	*1*	*1*	*0.99*	*0.98*	*0.94*	*0.86*	*0.76*	*0.71*	*0.65*
575°C	1	1	1	1	1	1	1	1	1	1	1	NA	NA
	1	*1*	*1*	*1*	*1*	*1*	*0.99*	*0.97*	*0.93*	*0.84*	*0.73*	*0.69*	*0.64*
600°C	1	1	1	1	1	1	1	1	1	1	1	NA	NA
	1	*1*	*1*	*1*	*1*	*1*	*0.99*	*0.96*	*0.91*	*0.82*	*0.72*	*0.68*	*0.63*
625°C	1	1	1	1	1	1	1	1	1	1	1	NA	NA
	1	*1*	*1*	*1*	*1*	*0.99*	*0.98*	*0.94*	*0.87*	*0.77*	*0.68*	*0.65*	*0.61*
650°C	1	1	1	1	1	1	1	1	1	1	1	NA	NA
	1	*1*	*1*	*1*	*1*	*0.99*	*0.97*	*0.91*	*0.83*	*0.72*	*0.64*	*0.61*	*0.58*

4 Summary

This report provides a summary on understanding and predicting the effects of long-term thermal aging on microstructure and tensile properties of G91 to corroborate the ASME Code rules in strength reduction due to elevated temperature service.

The thermal aging study of G91 involves three types of aged specimens: (1) specimens machined from two heats of G91, G91-H1 and H30176 that have been tested for the Advanced Materials Development Programs in the past years. These specimens were aged at 550, 600, and 650°C for times up to ~64,000 h; (2) specimens fabricated from the heads of the archived crept specimens (13 in total) of six heats of G91, H5349, H30394, H30383, H10148, H30176. These specimens were aged at 427 - 538°C and for times up to 132,647 h; (3) specimens made from a tube removed from the Kingston coal-fired power plant after exposure for 155,000 h at 550°C. These three sets of specimens provide a comprehensive data set for understanding and predicting the effect of long-term thermal aging on microstructure and tensile properties of G91.

Microstructural analysis of the thermally-aged G91 revealed that thermal aging causes significant microstructural changes: (1) the tempered martensite formed during tempering is unstable, and suffers significant recovery during aging, manifested by an increase in subgrain width, a decrease in subgrain length, and a decrease in subgrain aspect ratio (i.e. subgrains become more equiaxed) as the aging temperature and time increase. The subgrain recovery is facilitated by the reduction of dislocation density within subgrains; (2) $M_{23}C_6$ carbides in the as-received G91 are distributed along grain and subgrain boundaries and play an important role as pinning obstacles against subgrain coarsening. $M_{23}C_6$ carbides coarsen during aging, and the coarsening of $M_{23}C_6$ carbides reduces the pinning force on the boundaries; (3) MX carbonitrides in the as-received G91 are distributed uniformly within subgrains, providing the precipitation hardening effect. They coarsen with increasing aging temperature and time, but the coarsening rate is low; (3) a new phase, the Laves phase intermetallic forms during aging. The formation of the Laves phase removes the Mo solutes from the matrix, reducing the solid solution strengthening effect. The Laves phase particles grow rapidly once they are nucleated, and they precipitate primarily along boundaries. They may have a pinning effect on boundaries, but should provide little to the alloy strength. The evolution of each microstructural constituent during thermal aging can be well described by individual microstructural models. The estimated activation energy for MX coarsening was 175 kJ/mol, equivalent to the activation energy for boundary and core diffusion in α-Fe, while the estimated activation energy for subgrain coarsening was significantly lower, ~96 kJ/mol.

Thermal aging of G91 results in the reduction in the yield stress and the ultimate tensile strength but has an insignificant effect on the uniform and total elongations. The reduction in tensile strength is more pronounced as the aging temperature and time increases. The *in situ* tensile tests with high-energy X-rays revealed that sub-boundary strengthening plays a dominant role, and the strengthening role of $M_{23}C_6$ particles may be accounted for by subgrian boundary hardening, and three strengthening mechanisms can be superimposed to describe the tensile strength of G91: subgrain boundary hardening, MX precipitation hardening, and Mo solid solution strengthening. A microstructure – strength model was established to describe the effect of thermal aging on the yield and tensile strength of G91. The calculated yield stress – aging time and ultimate tensile

strength – aging time curves shows an excellent agreement with the experimental data. The model was then used to predict the yield and tensile strength reduction factors for thermally-aged G91 for the aging temperatures of 500 - 650°C with a 25°C interval for times up to 1×10^6 h (114 yr). The predicted values were compared with the yield and tensile strength reductions factors for times up to 3×10^5 h (34 yr) for G91 in ASME B&PV Code Section III, Subsection NH (new Division 5) Table NH-3225-2 and Table NH-3225-4. The predicted values are generally lower than the ASME Code values, and the differences become more significant at higher temperatures and longer times. It was predicted that G91 can retain ~70% of its initial tensile strength at the end life of 1×10^6 h at the service temperature of 500°C.

Acknowledgement

The research was sponsored by the U.S. Department of Energy, under Contract No. DE-AC02-06CH11357 with Argonne National Laboratory, managed and operated by UChicago Argonne LLC. Programmatic direction was provided by the Office of Nuclear Energy.

The authors gratefully acknowledge the support provided by Alice Caponiti, Director, Office of Advanced Reactor Technologies (ART), Sue Lesica, Federal Manager, ART Advanced Materials Program, Robert Hill of ANL, National Technical Director, ART Fast Reactors Campaign, and Sam Sham of ANL, ART Technology Area Lead on Advanced Materials.

Materials were provided by the Oak Ridge National Laboratory. D. L. Rink is thanked for specimen encapsulation. M. Quesinberry is thanked for maintaining furnaces and conducting tensile tests.

References

[1] R. Sandstrom, Acta Met. 25 (1977) 897.

[2] R. Sandstrom, Acta Met. 25 (1977) 905.

[3] Wagner R, Kampmann R. Homogeneous Second Phase Precipitation, in Haasen P (Ed.), Mater. Sci. Tech. Compr. Treat. Weinheim: Wiley-VCH; 1991.

[4] H. Ghassemi-Armaki, R.P. Chen, K. Maruyama, and M. Igarashi, J. Nucl. Mater. 433 (2013) 23.

[5] H. Ghassemi-Armaki, R.P. Chen, K. Maruyama, and M. Igarashi, Mater. Sci. Eng. A 527 (2010) 6581.

[6] H. Magnusson, R. Sandstrom, Metall. & Mater. Trans. A 38A (2007) 2033.

[7] Meimei Li, W. K. Soppet, D. L. Rink, and K. Natesan, Argonne National Laboratory, unpublished information, 2010.

[8] Meimei Li, D. L. Rink, W. K. Soppet, and K. Natesan, ANL-ARC-203, September 2011.

[9] I. M. Lifshitz and V. V. Slyozov, J. Phys. Chem. Solids 19 (1961) 35.

[10] C. Wagner, Z. Elektrochem 65 (1961) 581.

[11] H. J. Frost and M. F. Ashby: Deformation-Mechanism Maps: The Plasticity and Creep of Metals and Ceramics, (Pergamon Press, Oxford, 1982).

[12] Y. Hosoi, N. Wade, S. Kunimitsu, T. Urita, J. Nucl. Mater. 141-143 (1986) 461.

[13] A. Aghajani, F. Richter, C. Somsen, S.G. Fries, I. Steinbach, and G. Eggeler, Script. Mater. 61 (2009)1068.

[14] Meimei Li and Ken Natesan, Argonne National Laboratory, unpublished information, 2014.

[15] Meimei Li, Wei-Ying Chen, Xuan Zhang, and K. Natesan, Argonne National Laboratory, unpublished information, 2015.

[16] K. Maruyama, K. Sawada, and J. Koike, ISIJ Inter. 41 (2001) 641.

[17] K. Maruyama and H. Nakashima, 1997, Materials Science for High Temperature Strength, Uchida-Rokakudo, Tokyo, Japan.

[18] D. Peckner, The Strengthening of Metals, 1964.

[19] S. Takeuchi, Journal of the Physical Society of Japan 27 (1969) 929.

[20] S. V. Raj and G. Pharr, Mater. Sci. Eng. 81 (1986) 217.

[21] J. H. Schneibel and M. Heilmaier, Mater. Trans. 55 (2014) 44.

[22] E. Arzt, E. Gohring, Acta Mater. 46 (1998) 6575.

[23] I. Codd and N. J. Petch, Phil. Mag. 5 (1960) 30.

[24] K. Sawada, T. Ohba, H. Kushima, and K. Kimura, Mater. Sci. Eng. A 394 (2005) 36.

[25] W. Blum and X. H. Zeng, Acta Mater. 57 (2009) 1966.

Applied Materials Division
Argonne National Laboratory
9700 South Case Avenue
Argonne, IL 60439

www.anl.gov

Argonne National Laboratory is a U.S. Department of Energy
laboratory managed by UChicago Argonne, LLC